



Cite this: DOI: 10.1039/d6ce00054a

## Multiscale simulations of gas hydrates: from molecular mechanisms to mesoscale growth and macroscale flow and production predictions

 Miguel Pineda, <sup>\*a</sup> Anh Phan, <sup>\*b</sup> Michail Stamatakis <sup>a</sup> and Alberto Striolo <sup>cd</sup>

Gas hydrates—crystalline hydrogen-bonded water cages encapsulating gas molecules—are of major scientific and industrial interest for energy systems, safety and flow assurance, as well as for several emerging technologies. Predicting and controlling their formation, dissociation, and growth remains challenging due to coupled physical and chemical processes across multiple scales. This highlight article reviews recent advances in multiscale simulations of gas hydrates, from microscale mechanistic methods to mesoscale growth models and macroscale predictive simulators, and discusses how these approaches improve our ability to predict hydrate behaviour in natural and industrial settings. Current challenges are also discussed, together with suggestions for future research.

 Received 20th January 2026,  
 Accepted 23rd March 2026

DOI: 10.1039/d6ce00054a

[rsc.li/crystengcomm](https://rsc.li/crystengcomm)

### 1. Introduction

Gas (clathrate) hydrates are non-stoichiometric crystalline structures in which water molecules form hydrogen-bonds to yield cages encapsulating gas molecules.<sup>1–6</sup> These structures form under low-temperature and high-pressure conditions typically found in permafrost regions and in deep marine sediments along continental margins.<sup>7,8</sup>

Due to their wide distribution and structural diversity,<sup>9</sup> gas hydrates are considered a potential unconventional energy resource<sup>10,11</sup> and play key roles in marine geohazards<sup>12</sup> and climate processes.<sup>13</sup> In industrial settings, hydrate formation can obstruct pipelines and equipment, posing significant flow-assurance challenges.<sup>14,15</sup> Simultaneously, gas hydrates offer opportunities for gas storage and transport, including carbon dioxide (CO<sub>2</sub>) sequestration<sup>16,17</sup> and hydrate-based hydrogen storage,<sup>18</sup> and applications in wastewater treatment, seawater desalination,<sup>19,20</sup> separations, and cold thermal energy storage and refrigeration technologies.<sup>21</sup> Nevertheless, the practical deployment of applications based on hydrates remains limited because of an interplay of fundamental and technical challenges.

Toward overcoming these challenges, computational studies of gas hydrates provide an essential complement to experimental investigations because laboratory measurements are often limited by the pressure–temperature conditions required to form and stabilise hydrates, the difficulty of observing processes in buried marine sediments in the presence of various compounds, and the challenges of capturing nucleation and growth phenomena. The phenomena of interest evolve on diverse length- and time-scales, and various approaches focusing on specific aspects have been adopted: atomistic/molecular (micro)-scale models that describe cage formation and guest–host interactions,<sup>22,23</sup> mesoscale approaches that explore hydrate growth and agglomeration,<sup>24,25</sup> as well as macroscale models that address reservoir and flow assurance.<sup>14,26–28</sup> Gas hydrate phenomena are inherently multiscale, and a holistic integration and interpretation of these three levels of description are necessary to fully understand these systems.<sup>25,29–32</sup>

This article highlights recent advances in modelling hydrate nucleation, growth, transport, and reservoir behaviour, and stresses the need for cross-scale integration. Accordingly, the reviewed efforts toward achieving such integration are based on using molecular insights to inform mesoscale models and applying mesoscale results to guide reservoir simulations. Overall, these efforts strive toward coherent and predictive hydrate modelling that advances fundamental understanding and guides technology development.

While progress has been made across quantum, molecular, and continuum modelling in recent years, these advances remain partially fragmented across scales. Bridging these scales through multiscale computational tools,

<sup>a</sup> Department of Chemistry, Inorganic Chemistry Laboratory, University of Oxford, South Parks Road, Oxford, OX1 3QR, UK. E-mail: miguel.pineda@chem.ox.ac.uk

<sup>b</sup> School of Chemistry and Chemical Engineering, Faculty of Engineering and Physical Sciences, University of Surrey, Guildford, Surrey GU2 7XH, UK. E-mail: a.phan@surrey.ac.uk

<sup>c</sup> School of Sustainable Chemical, Biological and Materials Engineering, The University of Oklahoma, Norman, OK 73019, USA

<sup>d</sup> Materials Science and Engineering Program, The University of Oklahoma, Norman, OK 73019, USA



## Highlight

achieving predictive accuracy under realistic conditions, and obtaining comprehensive experimental validation is necessary to leverage fundamental understanding to overcome practical technological challenges.

The rest of the article is structured as follows: section 2 reviews microscale computational approaches; in Sec. 3, mesoscale modelling strategies are discussed; and in Sec. 4, macroscale simulators for reservoir and flow assurance applications are examined. Finally, in Sec. 5, conclusions and an outlook are presented.

## 2. Microscale molecular simulations

Microscale molecular simulations resolve guest–host interactions and water hydrogen-bond networks at the atomic level, providing fundamental insight into hydrate structure, cage occupancy, nucleation, and early growth. Guest–host

van der Waals (vdW) interactions<sup>36–40</sup> stabilise the three main cage-based structures (see Fig. 1)—sI, sII, and sH—whose behaviour depends on cage geometry, connectivity, and guest occupancy.<sup>33</sup> Density functional theory (DFT), grand canonical Monte Carlo (GCMC), and molecular dynamics (MD) simulations provide complementary perspectives on these processes, spanning electronic structure, thermodynamic stability, equilibrium cage occupancy, and non-equilibrium nucleation pathways.

### 2.1. Density functional theory applications

DFT studies have advanced our understanding of the molecular and structural stability of gas hydrates. As a quantum-mechanical electronic-structure method, DFT determines the ground-state electron density and total energy of hydrate systems within the framework pioneered by

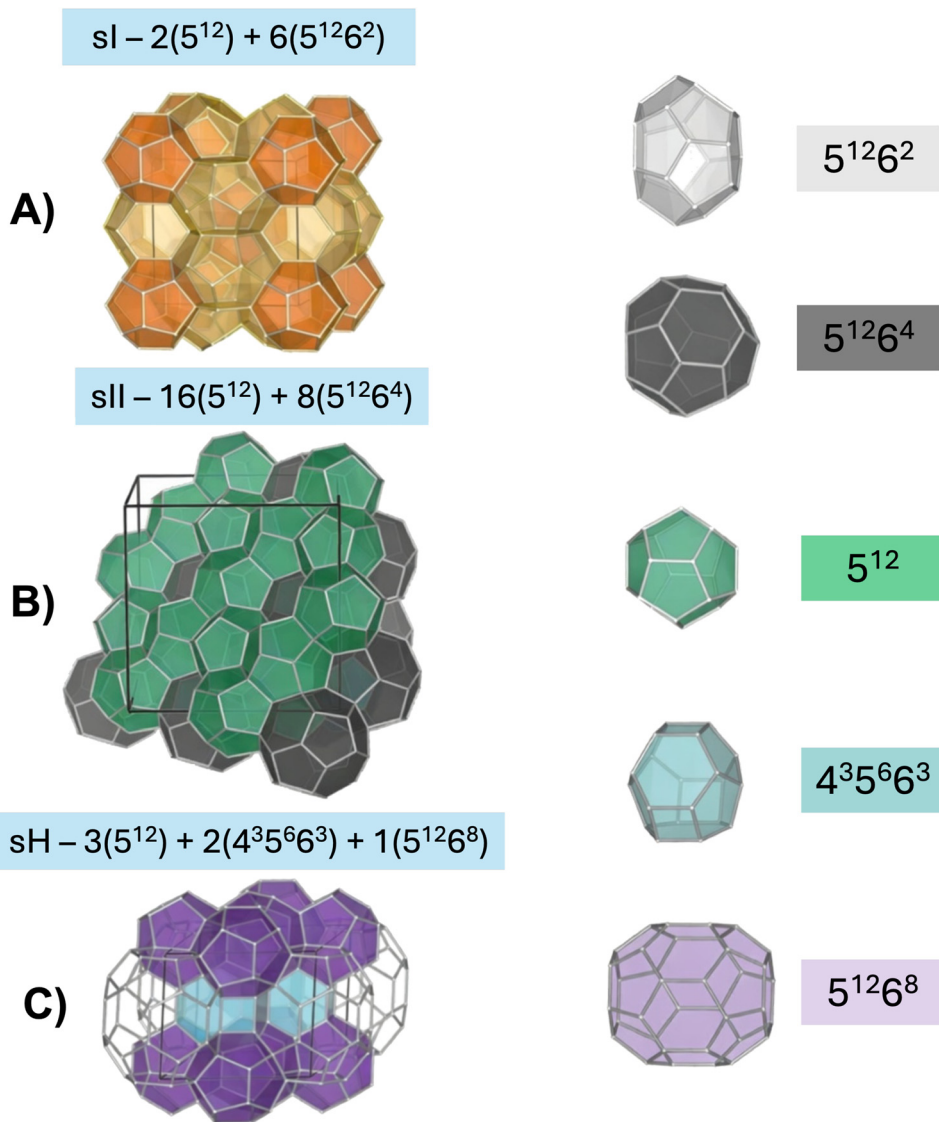


Fig. 1 Three main hydrate structures—sI (A), sII (B), and sH (C) with different host water cages. Adapted from Hassanpouryouzband *et al.*<sup>2</sup> Copyright © 2020 Royal Society of Chemistry.



Hohenberg and Kohn,<sup>41</sup> enabling quantitative evaluation of hydrogen bonding, dispersion-driven guest–host interactions, cage-occupancy effects, and pressure-dependent lattice stability.

By fitting equations of state to DFT energy–volume relations computed using the revised Perdew–Burke–Ernzerhof (revPBE) generalised-gradient approximation (GGA) exchange–correlation (XC) functional, Vlastic *et al.*<sup>42</sup> showed that the bulk modulus of sII hydrates scales linearly with hydrogen-bond density and that larger guest molecules increase lattice volumes through van der Waals (vdW)-driven cage expansion. Daghash *et al.*<sup>43</sup> performed extensive DFT calculations on sH hydrates using the revPBE GGA functional, complemented by vdW-DRSLL to assess dispersion effects, linking vibrational behaviour to elastic properties such as Young's modulus. The results highlighted an approximately linear dependence of elastic constants on pressure. Mathews *et al.*<sup>44</sup> found that SCAN-based DFT with rVV10 dispersion corrections predicts the thermodynamic properties of sI hydrates more accurately at low temperatures

than classical MD. Jendi *et al.*<sup>45</sup> quantified the compressive and tensile strengths of sI methane (CH<sub>4</sub>) hydrates using the revPBE functional without an explicit vdW correction, while Zhu *et al.*<sup>46,47</sup> used the revPBE functional with DFT-D2 dispersion corrections to confirm pressure-dependent elastic constants and the validity of the law of mixtures for sI CH<sub>4</sub> hydrates. These studies commonly assume uniform force distribution within stable lattices, though hydrate mechanics depend on interactions among the hydrogen-bond network and the connectivity between large and small cages.

Zhu *et al.*<sup>33</sup> combined DFT calculations (revPBE GGA with DFT-D2 vdW corrections) with a polyhedral composite framework to assess how cage occupancy governs pressure-induced failure of the hydrogen-bonded water lattice. Fig. 2A(left panel) shows lattice-volume changes from 0–7.6 GPa for four models: SELE (no cage occupancy), SOLE (small cages filled), SELO (large cages filled) and SOLO (all cages filled). At 0–4.5 GPa, all systems show similar, gradual volume reductions (<5%), indicating dominance of



**Fig. 2** A) Lattice volume versus hydrostatic pressure for four occupancy configurations: blue, orange, yellow, and purple lines correspond to SOLO, SELO, SOLE, and SELE hydrates (left). The 3D surface shows compressive stability limits versus phase occupancy;  $Q_l$  and  $Q_s$  denote large- and small-cage occupancies (right). Adapted from Zhu *et al.*<sup>33</sup> Copyright © 2023 Springer Nature. B) Methane C–H bending (left) and stretching (right) frequencies for different cage occupancies. Adapted from Schmidt *et al.*<sup>34</sup> Copyright © 2025 American Chemical Society.



hydrogen-bond forces over guest-host interactions. The unit lattice volumes agree well with previous DFT work (e.g., SOLO with  $\sim 1620 \text{ \AA}^3$  vs.  $1685 \text{ \AA}^3$  in Jendi *et al.*<sup>45</sup>). The SELE system fails at 4.6 GPa, marking the minimum compressive stability of the hydrogen-bonded lattice. Above 4.5 GPa, occupancy effects become pronounced. SOLO and SELO undergo major collapses at 7.3 and 6.4 GPa, respectively. SOLO is mechanically stronger than SELO, consistent with its fully occupied small cages. SELE and SOLE collapse earlier (4.6 and 4.9 GPa), indicating loss of structural integrity. The SOLO compressive limit (7.3 GPa) aligns with prior reports<sup>46,47</sup> ( $\sim 7.5$  GPa), supporting the accuracy of these results.<sup>33</sup> By analogy with the law of mixtures—replacing volumetric fractions with small- and large-cage occupancies, Zhu *et al.* expressed compressive stability  $S$  (GPa) as:  $S$  (GPa) =  $4.6 + 0.3Q_s + 1.7Q_l + 0.7Q_sQ_l$ , where  $Q_s$  and  $Q_l$  denote the fractional occupancies of small and large cages, respectively. The models predict stability limits to be in the pressure range 4.6 to 7.3 GPa, with SOLO being the most stable and SELE the least (see Fig. 2A, right panel).<sup>33</sup>

Among experiments useful to validate the computational predictions, infrared (IR) spectroscopy has been widely used to probe CH<sub>4</sub> hydrates properties. For example, the hydrogen-bond stretching frequency provides estimates of Young's modulus, while the number and frequencies of C–H stretching peaks reveal whether CH<sub>4</sub> occupies small cages, large cages, or both.<sup>34,48,49</sup> Computational work using VASP, SIESTA (Vibra), and CASTEP has reproduced hydrate vibrational spectra using either harmonic DFT-based calculations or classical MD simulations.<sup>50–53</sup> Schmidt *et al.*<sup>34</sup> used DFT with the rev-PBE-XC functional and DFT-D2 dispersion corrections to examine IR spectra of sI CH<sub>4</sub> hydrates at different occupancies. CH<sub>4</sub> exhibits two IR-active modes: C–H bending and asymmetric C–H stretching. Simulations reproduced these modes for both isolated CH<sub>4</sub> and CH<sub>4</sub> confined in hydrate cages. For isolated CH<sub>4</sub>, the modes appear at 1306 (bending) and 3048 (stretching) cm<sup>-1</sup> (see Fig. 2B), matching experiments at 1306 and 3019 cm<sup>-1</sup>.<sup>34</sup> The bending mode occurs at lower frequency than the bond stretching because angular deformation requires less energy than bond stretching. When encaged, both modes shift to higher frequencies, 1310 cm<sup>-1</sup> for bending and 3074 and 3089 cm<sup>-1</sup> for stretching, reflecting dispersion interactions with the surrounding water lattice. Splitting of each spectral band into several small peaks (10–15 cm<sup>-1</sup> apart) likely arises from slight differences in degenerate vibrational modes. Distinct C–H stretching peaks correspond to CH<sub>4</sub> in large ( $\sim 3074$  cm<sup>-1</sup>) and small ( $\sim 3089$  cm<sup>-1</sup>) cages, aligning with Raman results from Hansen and Berg.<sup>48</sup> The higher frequency and lower intensity of the small-cage peak indicate stronger confinement and fewer molecules per cage. Changing occupancy primarily alters peak intensities rather than positions, making the relative intensity of the C–H bending mode a useful indicator of overall occupancy.<sup>34</sup>

Cabrera-Ramírez *et al.*<sup>35</sup> investigated stability and occupancy patterns of sI CO<sub>2</sub> hydrates using dispersion-

corrected DFT-D methods, aimed at clarifying the transition from clathrate-like clusters to periodic crystals. They found that CO<sub>2</sub> binds more strongly within the large T (5<sup>12</sup>6<sup>2</sup>) cage than the small D (5<sup>12</sup>) cage (see Fig. 3A). This finding aligns with earlier studies based on both finite clathrate-like cluster models and periodic boundary simulations.<sup>54–59</sup> Estimated binding energies were  $-6.740$  kcal mol<sup>-1</sup> in T cages and  $-4.835$  kcal mol<sup>-1</sup> in D cages, giving an  $\sim 1.9$  kcal mol<sup>-1</sup> preference for large cages. Full occupancy of all eight cages stabilises the hydrate by  $\sim -51$  kcal mol<sup>-1</sup> relative to the empty lattice. Large-cage preference stems from the linear geometry of CO<sub>2</sub>: D cages impose more pronounced confinement and therefore stronger repulsive forces. Structurally, the D cage has twelve pentagons, while the T cage includes two hexagons and twelve pentagons, offering greater free volume. Single-crystal X-ray diffraction experiments at 173 K support these findings, showing full occupancy of T cages but partial filling of D cages.<sup>60</sup>

Recent experimental and theoretical studies<sup>54,55,57,59–62</sup> show that CO<sub>2</sub> molecules in sI clathrate cages adopt orientations allowing rotation. Cabrera-Ramírez *et al.*<sup>35</sup> also analysed the relaxed sI CO<sub>2</sub> structure and determined spatial orientations of guest CO<sub>2</sub> molecules (see Fig. 3B, top panel). They identified eight unique CO<sub>2</sub> positions: two in D cages and six in T cages (see Fig. 3B, bottom panel). In D cages, CO<sub>2</sub> aligns near the cage centre, consistent with experimental observations from single-crystal X-ray diffraction and neutron scattering, as well as with theoretical data by others.<sup>54,55,57,59–62</sup> In T cages, CO<sub>2</sub> orientations display broader angular variation, with  $\theta$  ranging between 75° to 100° and wide  $\phi$  distributions, with small positional shifts.<sup>60,61</sup> Cage connectivity governs intermolecular CO<sub>2</sub>–CO<sub>2</sub> separations in the sI hydrate: distances are shortest in TT(6) (5.77–6.14 Å), intermediate in DT (6.39–6.82 Å), and longest in TT(5) (6.95–7.44 Å) (see Fig. 3B). Short TT(6) separations suggest stronger guest–guest interactions mediated by the host lattice, whereas TT(5) distances indicate predominantly dispersion-driven CO<sub>2</sub>–CO<sub>2</sub> coupling. These results emphasise the combined role of cage geometry, guest orientation, and cage adjacency in stabilizing CO<sub>2</sub>-filled hydrates.

Valdés *et al.*<sup>72</sup> analysed translational-rotational states of CO<sub>2</sub> within sI hydrates using the multiconfiguration time-dependent Hartree method. They compared semiempirical and *ab initio* CO<sub>2</sub>–water potentials against DFT-D results and evaluated many-body influences on guest–host interactions.<sup>72</sup> Distinct excitation patterns were found to depend on the interaction model, reflecting subtle changes in CO<sub>2</sub> local structure within D and T cages. These results agree with neutron diffraction and <sup>13</sup>C NMR data<sup>60,61,73</sup> and predict previously unmeasured spectroscopic transitions, providing a benchmark for future studies.

The formation and stability of hydrates depend on fundamental guest–host and host–host interactions. Progress in this field requires a detailed understanding of these interactions and how they evolve under varying system



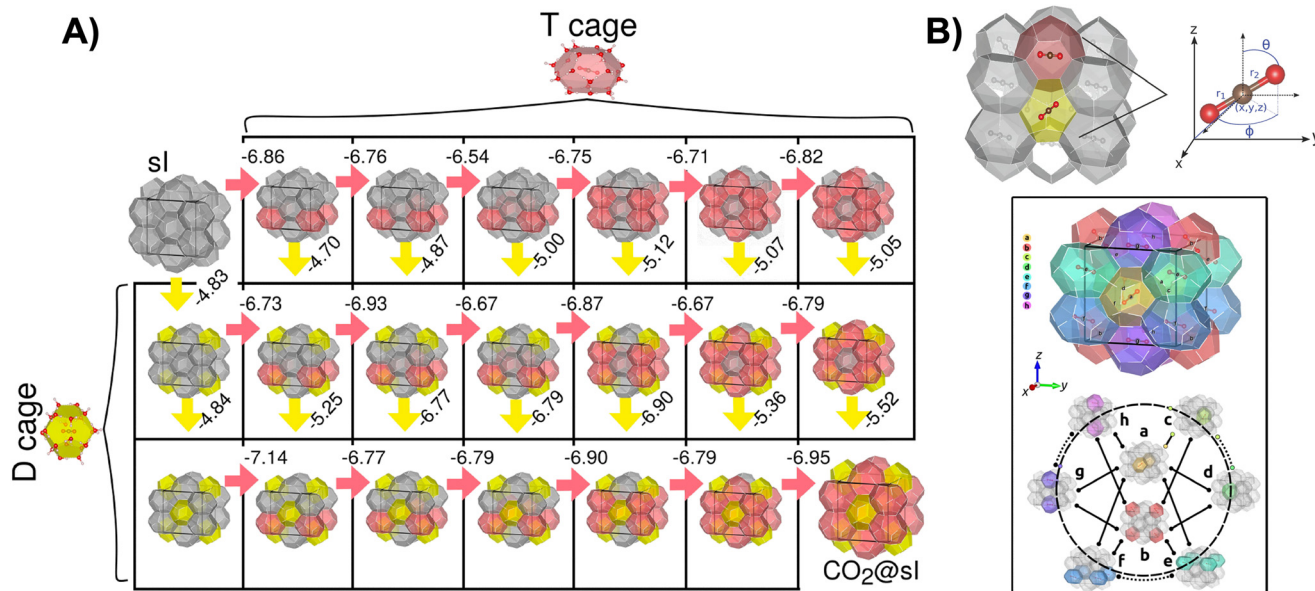


**Fig. 3** A) Progressive CO<sub>2</sub> occupancy in sI hydrate, with red (T) and yellow (D) cavities marking cages filled at each step. Binding energies (in kcal mol<sup>-1</sup> per added CO<sub>2</sub>) give the stabilization gained (negative) relative to the partially occupied structure and a free CO<sub>2</sub>. B) Top: sI CO<sub>2</sub> unit cell with D (yellow) and T (pink) cages and the DFT coordinate sites. Bottom: fully occupied sI CO<sub>2</sub> unit cell from periodic DFT showing DT (D-T), TT(6) (hexagon-sharing T-T), and TT(5) (pentagon-sharing T-T) connectivities. Cages a and b (D) connect to c-h (T) as DT pairs (solid); c-d, e-f, and g-h form TT(6) (dotted); other T-T pairs form TT(5) (dashed). Panels A) and B) adapted from Cabrera-Ramírez *et al.*<sup>35</sup> Copyright © 2021 John Wiley and Sons.

conditions. From a theoretical standpoint, accurately capturing guest–host interactions is computationally demanding, as it necessitates a consistent treatment of both the covalent and extended hydrogen-bond networks of the water framework and the noncovalent interactions between guest species and the host lattice. Although DFT can effectively describe guest–host interactions and predict equilibrium structures and pressure responses with reasonable computational efficiency,<sup>33–35,55,72</sup> the accuracy of both conventional and dispersion-corrected functionals in simultaneously representing hydrogen bonding and dispersion forces in gas hydrates must be carefully assessed. Consequently, systematic evaluations of key interaction effects, including cooperative guest–host interactions and guest–guest or cage–cage correlations, are necessary. Such understanding could help us better understand the thermal effects connected to the formation and dissolution of hydrates, one of the main challenges for the technological deployment of these systems. Capturing the full thermodynamic behaviour of clathrate hydrates requires explicit treatment of temperature- and pressure-dependent effects through molecular-scale simulations capable of resolving cavity occupancy and cooperative interactions.

## 2.2. Grand canonical Monte Carlo simulations

GCMC simulations are widely used to investigate guest adsorption and cage occupancy in gas hydrates under fixed temperature, volume, and chemical potential conditions.<sup>74–78</sup>

In this framework, particle insertion, deletion, translation, and rotation moves are performed to sample equilibrium configurations of guest molecules within a pre-defined (often rigid) hydrate lattice. GCMC calculations enable the efficient study of adsorption thermodynamics and cage occupancy distributions on much shorter timescales than MD, where evaluating occupancy requires guest diffusion through hydrate cages, a notoriously slow process. When combined with van der Waals–Platteeuw (vdWP) theory,<sup>6,79</sup> GCMC enables the evaluation of hydrate phase equilibria across diverse compositions.

To provide a fundamental underpinning for developing new processes that, for example, replace CH<sub>4</sub> in natural hydrates with CO<sub>2</sub>, it is essential to understand hydrate stability as a function of guest type and occupancy.<sup>62,80–86</sup> Phase-equilibria and composition-evolution studies,<sup>80,87,88</sup> supported by spectroscopic evidence,<sup>62,82,84,86,89</sup> show that CO<sub>2</sub> preferentially replaces CH<sub>4</sub> in the large sI cages due to size compatibility. However, the behaviour of mixed CO<sub>2</sub>–CH<sub>4</sub> hydrates remains debated.

Qiu *et al.*<sup>63</sup> combined GCMC with MD simulations to investigate the adsorption isotherms of pure and mixed CH<sub>4</sub>–CO<sub>2</sub> hydrates using different guest and host models. Their CH<sub>4</sub> cage occupancy results for sI and sII hydrates were compared with earlier stand-alone Monte Carlo (MC) simulation conducted at 270 K<sup>64–67</sup> and with experiments at 268–271 K<sup>68–71</sup> (see Fig. 4A). Simulations employing the TIP4P/Ice water model produced higher occupancies than those using TIP4P/Ew, owing to stronger host–guest interactions—overestimating small-cage occupancy but





Fig. 4 A) Pressure dependence of CH<sub>4</sub> occupancy in large (left) and small (right) sI cages at ~270 K. Red, blue, and black symbols correspond to Qiu *et al.*,<sup>63</sup> previous simulations,<sup>64–67</sup> and experiments.<sup>68–71</sup> B) Temperature- and pressure-dependent occupancy ratios  $\theta_L/\theta_S$  for CH<sub>4</sub> (left) and CO<sub>2</sub> (right) in sI and sII hydrates;  $\theta_L$  and  $\theta_S$  denote fractions of large and small cages filled. Panels A) and B) adapted from Qiu *et al.*<sup>63</sup> Copyright © 2018 American Chemical Society.

accurately capturing large-cage occupancy in the sI hydrate.<sup>63</sup> Flexible hydrate models yield lower occupancies than rigid ones because cage distortion hindered guest entry. With flexible hydrate and united atoms (UA) CH<sub>4</sub> models, Qiu *et al.*<sup>63</sup> closely replicated the experimentally observed small-cage occupancies (Fig. 4A, right panel), though large-cage (Fig. 4A, left panel) values were slightly underestimated. Similar trends were observed with UA0.88 and all-atom (AA) CH<sub>4</sub> models, which matched small-cage data from Klapproth *et al.*<sup>70</sup> but underestimated total occupancies. These results highlight the strong dependence of hydrate occupancy on lattice and water models, with greater accuracy expected from rigid lattices and TIP4P/Ice model. The total occupancy obtained using TIP4PEw and DACNIS-UA<sup>90</sup> models aligned more closely with experimental data than earlier TrapPE-UA predictions. Overall, both experimental and GCMC simulation results<sup>63–71</sup> confirm that CH<sub>4</sub> preferentially occupies large cages, consistent with DFT predictions linking cage occupancy to the stability of sI CH<sub>4</sub> hydrates.<sup>33</sup>

Qiu *et al.*<sup>63</sup> reported that in sI and sII hydrates, the occupancy ratio of CO<sub>2</sub> and CH<sub>4</sub> between large and small cages ( $\theta_L/\theta_S$ ) decreases under higher pressures but increases with temperature (see Fig. 4B), consistent with both experiments<sup>91</sup> and earlier simulations.<sup>65,92</sup> The  $\theta_L/\theta_S$  ratio is higher in sII than in sI due to the greater size contrast between their cages. At sufficiently high pressures,  $\theta_L/\theta_S$  approaches 1.0 from above, indicating that small cages fill after large ones. For sI CH<sub>4</sub> hydrate at 270 K and 6 MPa, calculated  $\theta_L/\theta_S$  values (1.40 and 1.16 for the AA and UA model, respectively) (see Fig. 4B, left panel) align well with experimental data (~1.26 at 270 K<sup>84</sup> and 1.13–1.15 at 268 K).<sup>68–71</sup> For CO<sub>2</sub>,  $\theta_L/\theta_S$  is significantly larger at low pressures—about 3.13 and 5.13 for sI and sII at 270 K and 1.5 MPa (see Fig. 4B, right panel)—implying that large cages are preferentially occupied. These results agree reasonably with experimental (8.33 at 1.2 MPa and 273 K)<sup>93</sup> and vdW-Platteeuw thermodynamic values (1.91 and 1.35),<sup>94</sup> confirming that the GCMC + MD simulations reliably capture CO<sub>2</sub> and CH<sub>4</sub> adsorption behaviour in hydrates, while



additionally resolving cage-specific occupancy, local heterogeneity, and molecular-scale adsorption mechanisms that are not directly accessible experimentally.

Unlike the classical vdWP theory, GCMC does not require assumptions regarding the number of guest molecules per cavity. In GCMC simulations, cavity occupancies emerge naturally from the calculations. In addition, GCMC explicitly accounts for guest-guest interactions, alongside guest-host interactions with the water lattice. Despite these advantages, GCMC cannot assess the thermodynamic stability of hydrate crystals, which must be assumed *a priori*. Moreover, predicted phase equilibria are highly sensitive to the choice of force fields, necessitating careful validation against experimental data. Finally, as a MC technique, GCMC provides not insight into hydrate nucleation and growth kinetics.

### 2.3. Molecular studies of hydrates nucleation and growth

By tracking the position over time of individual atoms and molecules, MD simulations reveal their assembly into hydrate

structures, providing a powerful framework for understanding inhibitor effects and hydrate growth across environments. In classical MD, forces are described by empirical force fields, enabling nanosecond to microsecond simulations, whereas *ab initio* MD (AIMD) derives forces from DFT calculations, offering higher accuracy at substantially greater computational cost. Coarse-grained MD (CGMD) reduces molecular detail to access longer time and length scales. MD simulations provide insights into nucleation mechanisms,<sup>95,98–100</sup> growth dynamics,<sup>97,101,102</sup> and the influence of additives<sup>22,103–105</sup> and confinement<sup>106,107</sup>—often beyond experimental reach.

Several conceptual scenarios had been proposed to explain the nucleation mechanism. In 1991, Sloan and Fleyfel introduced the labile cluster hypothesis (LCH), which suggested that water molecules form transient, cage-like structures around guest molecules that subsequently merge to form hydrate crystals.<sup>108</sup> Later classical MD and MC simulations demonstrated that isolated clathrate cages are rare, extremely short-lived, and energetically unstable in



**Fig. 5** A) Simulation snapshots and cage-type evolution during induction, nucleation, and growth; inset shows early nucleation. Violet, green, black, and yellow denote  $5^{12}$ ,  $5^{12}6^2$ ,  $5^{12}6^3$ ,  $5^{12}6^4$  cages. Adapted from Walsh *et al.*<sup>95</sup> Copyright © 2009 AAAS. B) Interaction energy ( $E_{\text{in}}$ ) of adsorbed water versus water count in small (blue) and large (red) cages. Adapted from Liu *et al.*<sup>96</sup> Copyright © 2016 Elsevier. C) Temporal evolution of  $5^{12}$  (blue) and  $5^{12}6^2$  (red) cages in  $\text{sI}$  CH<sub>4</sub> hydrate without additives (left) and with two SDS molecules (middle), and free-energy profiles (right) for CH<sub>4</sub> transfer from hydrocarbon to aqueous phase. Systems: SDS at low (green) and high (red) coverages and without SDS (blue). Adapted from Phan *et al.*<sup>97</sup> Copyright © 2023 Elsevier.



## Highlight

solution.<sup>109,110</sup> Further studies showed that guest-filled cages are more likely to disintegrate than aggregate, and that fully enclosed polyhedral cages form only at very high guest concentrations with very low probability.<sup>109,110</sup> Although cage stability can increase in the presence of multiple guest molecules, these findings indicate that hydrate nucleation does not proceed *via* isolated cages. Consequently, the local structuring hypothesis was proposed, suggesting that hydrate nucleation is governed by local concentration fluctuations that organise guest molecules into hydrate-like configurations. Achieving these configurations is the rate-limiting step in crystal formation. A historical overview of hydrate nucleation studies is provided in the work of Zhang *et al.*<sup>111</sup>

A pioneering MD simulation study of hydrate nucleation was conducted by Walsh *et al.*,<sup>95</sup> who found that five water molecules and two CH<sub>4</sub> molecules jointly organise into a stable pentagonal water ring that persists during transient cavity formation. This CH<sub>4</sub>-water cooperation facilitates further ordering and CH<sub>4</sub> adsorption, in line with earlier works showing that CH<sub>4</sub> stabilises hydrate faces.<sup>112,113</sup> Under the super-saturated conditions considered in these simulations, a small (5<sup>12</sup>) cage emerged at 1.225 μs (Fig. 5A), surrounded by a CH<sub>4</sub> layer. Steric constraints prevent extended growth of face-sharing 5<sup>12</sup> cages until the central cage opens after ~30 ns, enabling rearrangement and rapid expansion. Over ~240 ns, the 5<sup>12</sup> cage evolved into a 5<sup>12</sup>6<sup>3</sup> cage—a transitional motif connecting sI and sII hydrates. Similar rearrangements appear elsewhere, producing mixed sI-sII networks. Walsh *et al.*<sup>95</sup> showed that 5<sup>12</sup> cages dominate early nucleation, followed by 5<sup>12</sup>6<sup>2</sup> (sI) cages after ~100 ns, consistent with the thermodynamic stability of sI hydrates. Larger 5<sup>12</sup>6<sup>4</sup> (sII) cages remain rare,<sup>1</sup> forming transiently due to adjacent small-cage patterns. The 5<sup>12</sup>6<sup>3</sup> cages act as structural links, promoting sI formation from sII-like clusters (see Fig. 5A). The final hydrate contains mixed sI/sII motifs, consistent with experimental<sup>114-116</sup> and simulation results<sup>117,118</sup> showing that early nucleation generates heterogeneous structures stabilised by shared 5<sup>12</sup> cages. The apparent discrepancy with DFT studies highlighting large-cage occupancy as the primary stability factor<sup>33,35</sup> likely reflects the non-equilibrium nature of MD simulations, which capture early-stage nucleation under highly supersaturated conditions.<sup>95</sup>

Liu *et al.*<sup>96</sup> used AIMD to examine the assembly of hydrogen-bonded cages in sI CH<sub>4</sub> hydrates. They found that small cages originate from pentagonal water rings hosting one CH<sub>4</sub> molecule, whereas large-cage precursors form from hexagonal water rings—consistent with results reported by Walsh *et al.*<sup>95</sup> However, the formation mechanisms differ: small cages grow through ring expansion (ternary → quaternary → pentagonal), while large cages assemble through a layer-separated process, as surrounding water molecules are more strongly attracted to the large-cage precursor and experience less CH<sub>4</sub> repulsion. These findings support a two-step formation process: (1) local water ordering

forms precursors, and (2) CH<sub>4</sub>-driven restructuring produces hydrate cages. Small 5<sup>12</sup> cages preferentially form in early nucleation due to stronger interactions between adsorbed water and the cage structure (Fig. 5B). Large 5<sup>12</sup>6<sup>2</sup> cages later dominate sI hydrates because of their higher energetic favourability.<sup>96</sup>

AIMD simulations are typically limited to short trajectories. It is therefore encouraging that, using non-equilibrium MD simulations, Phan *et al.*<sup>97</sup> found that the formation rate of 5<sup>12</sup>6<sup>2</sup> cages (~43–51 cages per ns) is nearly three times higher than that of 5<sup>12</sup> cages (~15 cages per ns). This corresponds to a 1:3 ratio of 5<sup>12</sup> to 5<sup>12</sup>6<sup>2</sup> cages, indicating domination of the 5<sup>12</sup>6<sup>2</sup> cages in the sI hydrate structure, in good agreement with the AIMD study conducted by Liu *et al.*<sup>96</sup> Phan *et al.* demonstrated that it is possible to quantify the effect of chemical additives on hydrate growth, reporting that the introduction of two sodium dodecyl sulfate (SDS) molecules (0.06 molecules per nm<sup>2</sup>) significantly accelerates sI hydrate growth (Fig. 5C, left panel). This observation is consistent with experiments showing that low SDS concentrations enhance CH<sub>4</sub> hydrate growth at CH<sub>4</sub>-water interfaces, increasing growth rates from 1.18 to 1.55 mm s<sup>-1</sup> at 4 MPa and 273 K.<sup>119</sup> Both simulations<sup>105</sup> and experiments<sup>119</sup> identify SDS as an efficient promoter at hydrocarbon-water boundaries. However, increasing SDS to twelve molecules (0.36 molecules per nm<sup>2</sup>) yields little additional acceleration.<sup>97</sup> These results indicate that additives in curved interfaces influence CH<sub>4</sub> solubility and thereby growth rates.<sup>22,100</sup> Through thermodynamic analysis, Phan *et al.*<sup>97</sup> proposed that combining potential-of-mean-force metrics—binding free energy ( $\Delta G_{\text{bind}}$ ) and adsorption barrier ( $\Delta G_{\text{barrier}}$ )—with interfacial deformation energy ( $\Delta G_{\text{def}}$ ) (Fig. 5C, right panel) enables prediction of additive performance, supporting the design of hydrate-based CH<sub>4</sub> storage systems. Cai *et al.*<sup>120</sup> further showed that SDS can form micellar aggregates with other chemicals, such as tetrahydrofuran (THF), leading to antagonistic effects on hydrate growth kinetics, in agreement with calorimetry experiments.

MD simulations with a hydrate seed enable the identification of the mechanisms of action of thermodynamic promoters. Using this approach, Economou and co-workers reproduced experimental properties of CH<sub>4</sub> hydrates,<sup>121,122</sup> while Phan *et al.*<sup>101</sup> showed that THF promotes CO<sub>2</sub> hydrates. Cai *et al.*<sup>123</sup> further demonstrated that dioxane stabilizes sII hydrates in which CH<sub>4</sub> can occupy both small and large cages, which grow *via* direct and indirect mechanisms and some cages remaining empty. These findings inform the potential of hydrate-based natural gas storage because sII hydrates offer larger cage where CH<sub>4</sub> can be stored, compared to sI hydrates, reducing the amount of water necessary to store a given amount of CH<sub>4</sub>. However, CH<sub>4</sub> alone does not stabilize sII hydrates - other guests are needed, and it is imperative to prevent those guests from occupying the large cages, which would defeat the purpose of enhancing CH<sub>4</sub> storage capacity.



Returning to nucleation, previous simulations show that  $5^{12}$  cages form early in nucleation only for small guests.<sup>95,118,124–126</sup> Larger species such as THF, propane, and ethane cannot enter these cages and form hydrates with only large cages filled. Jacobson *et al.*<sup>98</sup> used CGMD to show that guest size governs nucleation pathways: small (S), medium (M), large (L), and extra-large (XL) guests stabilize sII, sI, psI, and psII structures, respectively (where the p designates a partially filled structure with empty  $5^{12}$  cages). Without guests, sII is more stable than sI due to reduced structural strain.<sup>127</sup> Small guests occupy both cage types in sII; medium-sized guests favour sI, filling both  $5^{12}$  and  $5^{12}6^2$  cages; large guests occupy only the large cages of sI or sII; and XL guests occupy only the largest cages. Fig. 6A shows how guest size governs stabilization: S and M favour  $5^{12}$  cages, whereas M-sized ( $\text{CH}_4$ -like) guests preferentially stabilize  $5^{12}6^2$  cages, in line with DFT calculations<sup>33–35</sup> and AIMD simulations.<sup>96</sup>

Jacobson *et al.*<sup>98,128</sup> proposed an innovative method to compare the stability of various hydrate structures. As a first-order estimate of their free energies, the enthalpies of formation of sI, sII, psI, and psII hydrates were evaluated, and a stability phase diagram was obtained (see Fig. 6B).<sup>98</sup> Direct melting simulations were then employed to refine these predictions. At approximately 50.7 MPa, the stable

phases were identified as sII for S guests, sI for M guests, psI for L guests, and psII for XL guests. Only the latter two cases differ from the phase stability diagram predictions.<sup>128</sup> S guests (*e.g.*, Ar) fill both cages in sII; M guests ( $\text{CH}_4$ ,  $\text{CO}_2$ ) form sI with both cages filled;<sup>126,128</sup> L guests such as trimethylene oxide occupy only large  $5^{12}6^2$  cages in sI;<sup>1</sup> and XL guests like THF form sII with only large  $5^{12}6^4$  cages occupied.<sup>98</sup> These results confirm that guest size is a key descriptor for hydrates stability. Guest size is also a key descriptor for the nucleation pathways. In fact, Jacobson *et al.*<sup>98</sup> identified multiple competing nucleation pathways involving filled or empty  $5^{12}$  cages and various  $5^{12}6^n$  cages. For  $\text{CH}_4$ , nucleation is dominated by filled  $5^{12}$  cages,<sup>95,124</sup> whereas empty  $5^{12}$  cages provide secondary channels. When guests are too large to occupy the  $5^{12}$  cages, nucleation proceeds through combinations of vacant  $5^{12}$  cages and occupied  $5^{12}6^n$  cages; medium-sized guests mainly fill the large cages, while XL guests occupy only the largest ones (see Fig. 6C).<sup>98</sup> Empty  $5^{12}$  cages are stabilized by nearby solvating guest molecules, requiring at least three; filled cages can form with minimal solvation. The abundance of guest-filled large cages in the critical nuclei arises from kinetic (hydration similarity) rather than thermodynamic preference.<sup>98</sup> This highlights the central role of water reorganization in the first hydration shell. It should be noted that, to accelerate nucleation, gas hydrate MD simulations are often conducted under supercooled and/or supersaturated conditions, under which critical nuclei may differ in structure and composition from stable or metastable hydrate phases.<sup>98</sup>

Many hydrate-based technologies are limited by slow growth and dissolution kinetics, motivating the development of kinetic promoters. Among them, environmentally friendly compounds such as tryptophan significantly enhance  $\text{CH}_4$  hydrate growth by thickening the quasi-liquid water layer at the hydrate-liquid interface, thereby facilitating guest transport and incorporation,<sup>129</sup> consistent with mechanisms proposed by Phan *et al.*<sup>130</sup> One question to be addressed here is how to identify new effective promoters that are effective at low concentrations while being environmentally benign and economically affordable.

MD simulations can help address this quest, but their practical application remains limited by time- and length-scale constraints. As a result, many phenomena bridging microscopic and meso- or macro- scale scales cannot be directly captured. In addition, simulations differ fundamentally from experiments in how temperature and pressure are controlled: thermostats and barostats rapidly remove the heat released during hydrate nucleation and growth, unlike experimental systems. Although microcanonical simulations can account for heat transfer, they cannot simultaneously control pressure and often suffer from excessive temperature rises due to small system sizes. Consequently, faithfully reproducing experimental hydrate formation *via* MD remains challenging. Furthermore, current force fields have limitations and reproduce only selected



Fig. 6 A) Normalized per-water-guest interaction energy versus the guest-water size parameter  $\sigma_{ws}$ . Colours indicate  $5^{12}$  (green),  $5^{12}6^2$  (blue),  $5^{12}6^3$  (red), and  $5^{12}6^4$  (orange) cages. Vertical dashed lines mark the  $\sigma_{ws}$  of the four model guests and their favoured cages. B) Stability domains of sI, sII, psI, and psII as functions of  $\sigma_{wm}$  (same as  $\sigma_{ws}$  in A) and  $\epsilon_{wm}$  (same as  $\epsilon_{ws}$  in A);  $n_w$  is the water count per cage. C) Representative nuclei for S, M, and XL guests: S fills all cages, M mainly large, XL only large. Panels A), B), and C) adapted from Jacobson *et al.*<sup>98</sup> Copyright © 2010 American Chemical Society.



molecular properties; for example, while TIP4P/Ice accurately describes the triple point for water and hydrate phases, TIP4P/2005 better represents condensed water phases. While the discussion so far considered hydrates growth, to release the guests once trapped in the hydrate cages, it is necessary to dissolve the hydrates. The relevant mechanisms are different than those responsible for growth, and must be understood to facilitate practical applications.

Collectively, DFT, GCMC, and MD simulations form a coherent framework for understanding hydrate formation and stability. However, their predictive capability remains constrained by the accuracy of XC functionals in DFT and the fidelity of classical force fields in GCMC and MD simulations, as well as by the intrinsic difficulty of sampling rare events. Recent advances in machine learning (ML)-based force fields

offer promising routes to improved accuracy at a reasonable computational cost. Parallel developments in ML-assisted DFT, particularly the construction of data-driven XC functionals, provide a promising route to improving the accuracy of DFT predictions for gas hydrate energetics, host-guest interactions, and phase stability.

### 3. Mesoscale gas-hydrate phenomena

Microscale processes control hydrate nucleation and early growth,<sup>4,22,23</sup> whereas subsequent growth and environmental interactions are governed by mesoscale heat and mass transfer coupled with pore-scale dynamics.<sup>25</sup> The mesoscale domain—typically spanning  $\sim 100$  nm to  $100$   $\mu\text{m}$  and timescales from ms to s—bridges molecular phenomena with



Fig. 7 A) CA lattice of Pineda *et al.*<sup>24</sup> composed of cubic voxels ( $V = l^3$ ): hydrate-crystal (diagonally hashed cells), hydrate-water interface (red dashed), and other voxels (black). The interface advances as voxels switch between liquid-like (water + dissolved  $\text{CO}_2$ ) and solid ( $\text{CO}_2$  hydrate). B) Spatiotemporal evolution of sl  $\text{CO}_2$  hydrate grown from a seeded thin film into  $\text{CO}_2$ -saturated water at various subcoolings  $\Delta T$ , all at  $t = 24$   $\mu\text{s}$  (common colour bars). Panels A) and B) adapted from Pineda *et al.*<sup>24</sup> Copyright © 2023 The Authors. Published by the American Chemical Society under CC-BY 4.0.



field-scale behaviour. At this scale, hydrate systems exhibit emergent behaviour arising from coupled transport and phase-change processes, necessitating spatially resolved continuum or stochastic modelling approaches. Mesoscale frameworks capture morphology evolution, transport behaviour, and particle-size dynamics. Cellular automata (CA), lattice Boltzmann modelling (LBM), phase-field (PF), and population balance (PB) methods each address complementary aspects of mesoscale hydrate behaviour.

### 3.1. Cellular automata modelling

The CA method was one of the first spatially resolved simulation approaches developed to study solidification (*e.g.*, dendritic growth and grain evolution).<sup>131</sup> It represents complex systems as networks of cells whose state variables evolve according to deterministic or probabilistic rules and effectively captures emergent behaviour arising from local interactions and molecular phenomena such as those described above for hydrates.<sup>132</sup>

Buanes *et al.*<sup>133,134</sup> developed a probabilistic CA that was a hybrid between MC and CA methods to simulate the growth of CO<sub>2</sub> hydrates, where cells switch between liquid and solid states based on minimization of free energy and probabilistic rules, with the diffusion of CO<sub>2</sub> and heat treated explicitly. Their results showed that hydrate growth is primarily diffusion-limited, producing compact crystals at low supersaturation and dendritic structures at high supersaturation. The temperature effects were minor, except under large supersaturation conditions.

Pineda *et al.*<sup>24</sup> extended the MC-CA framework to model si CO<sub>2</sub> hydrate growth from an already formed thin film into stagnant CO<sub>2</sub>-saturated water. Phase transitions, interfacial attachment kinetics, and diffusion are incorporated in the model (see Fig. 7A). The model predicts that low subcooling leads to planar fronts, while higher subcooling destabilizes growth through the Mullins–Sekerka instability<sup>135</sup> and produces needle-like and dendritic morphologies (see Fig. 7B). These results are consistent with experiments.<sup>136</sup> The framework by Pineda *et al.* was designed with computational efficiency in mind, making it well-suited for future integration into multiscale applications. This level of analysis seems very promising, and it would benefit from the direct inclusion of molecular phenomena - for example, what is the fate of the additives used to promote hydrate growth? Can this fate affect the macroscopic performance?

Jahangiri and Varaminian<sup>137</sup> recently introduced a hybrid CA-finite difference (FD) model for THF hydrate formation at atmospheric pressure. The FD scheme captures transient heat transfer, while probabilistic CA rules govern local phase change. The model reproduces experimental temperature fields and growth kinetics and underscores the influence of surface cooling and initial solution temperature on hydrate growth.

The above examples show that CA modeling for gas hydrates is a promising and versatile approach, yet it faces

important challenges. Its dependence on probabilistic transition rules based on free-energy differences or empirical acceptance functions may limit the accurate description of crystallization kinetics. Moreover, although CA models can reproduce key morphologies—such as planar growth fronts, needle-like structures, and dendritic instabilities—the validation of these predictions remains limited by the scarcity of well-controlled experimental data.<sup>136,138</sup>

### 3.2. Lattice Boltzmann modelling

The LBM approach was developed as a mesoscopic approach for simulating fluid flow and has since been extended to model multiphase phenomena. It recovers macroscopic hydrodynamic behaviour from simplified kinetic equations defined on a lattice, making it particularly well-suited systems in which the geometry, albeit complex, is well defined, as is the case for hydrates. LBM is especially advantageous for porous media applications, where pore-scale geometry controls multiphase flow and permeability evolution in hydrate-bearing sediments. The inherently local structure of the LBM enables efficient parallel implementation, offering significant computational benefits.<sup>140</sup>

Back in 2004, Kang *et al.*<sup>141</sup> first modelled crystal growth in supersaturated pure water as a first step towards simulating hydrate formation and decomposition. Although not applied to gas hydrates, the proposed two-dimensional (2D) LBM framework showed that the interaction between diffusion, surface reaction, and nucleation density governs the morphology and growth kinetics of crystals. Specifically, diffusion-controlled growth resulted in open dendritic (cluster-like) structures, while reaction-controlled growth produced compact, circular crystals.

Wang *et al.*<sup>142</sup> applied a similar LBM framework directly to the formation of cyclopentane hydrates in brine. Cyclopentane offers promising applications in hydrate-based desalination because it can readily form hydrates in brine at atmospheric pressure and at temperatures above the freezing point of water.<sup>143</sup> Their 2D-LBM kinetic model incorporated convection and diffusion of both guest molecules and salt ions, plus the salt exclusion effects and salinity-dependent kinetics, and predicted that hydrate morphology strongly depends on the diffusion length of the guest molecule, but only weakly on salinity. The predicted water conversion under a wide range of salinity conditions was found to be in good agreement with the experimental measurements.<sup>144</sup>

The evolution of permeability in hydrate-bearing sediments, which likely depends on the formation of hydrates within the pore network, is critically important for assessing natural gas production potential from hydrate deposits, as the presence, distribution, and dissociation of gas hydrates directly control gas and water flow through porous media, thereby governing reservoir productivity and stability. LBM studies have demonstrated that permeability is not solely determined by hydrate saturation, but depends





**Fig. 8** A) Grain-coating (left), pore-filling (middle), and dispersed (right) hydrate morphologies with sand grains (red), hydrate (green), and pore space (blue), all starting at 50.72% hydrate saturation in a 2.24 mm  $\times$  2.06 mm sample on a 224  $\times$  206 lattice. B) LBM-predicted normalized permeability ( $K_{\text{hyd},g}$ ) versus hydrate saturation ( $S_{\text{hyd}}$ ) for isothermal (left), depressurization (middle), and depressurization with thermal stimulation (right), with simulations run to full dissociation; each point shows saturation and corresponding permeability. Panels A) and B) adapted from Li *et al.*<sup>139</sup> Copyright © 2024 Elsevier.

also on the growth habit of the hydrate,<sup>145,146</sup> wettability and microscale blocking effects,<sup>147</sup> and the type of sediment.<sup>148</sup> LBM simulations on microcomputed tomography images have confirmed that hydrate distribution can drastically alter flow pathways.<sup>149,150</sup>

Li *et al.*<sup>139</sup> developed a coupled hydrodynamic-thermal LBM framework and showed that the evolution of permeability in hydrate-bearing sediments during the dissociation of hydrates strongly depends both on the hydrate morphology and the dissociation conditions. Their results, illustrated in Fig. 8, demonstrate that thermal stimulation enhances pore connectivity and leads to a nearly linear increase in permeability in heterogeneous sediments. This finding is relevant because hydrate dissociation is endothermic:<sup>139</sup> thermal stimulation supplies the additional heat required to accelerate dissociation and to promote the early formation of interconnected flow pathways, which drive the changes in permeability.

LBM simulations have demonstrated that hydrate dissociation can be limited by either mass transfer or heat transfer, depending on local conditions.<sup>151–154</sup> LBM investigations have also been extended to explicitly account for ice formation at sub-freezing temperatures,<sup>155</sup> the dissociation of CO<sub>2</sub> hydrates for energy storage

applications,<sup>156</sup> the impact of thermal fluid injection and multi-field coupling,<sup>157</sup> as well as realistic hydrate dissociation pathways in rock matrices.<sup>158</sup>

The LBM is a powerful tool for hydrate research. However, it is inherently restricted to the pore scale and does not directly yield Darcy's law.<sup>159</sup> Therefore, the development of robust and generic LBM frameworks to connect pore-scale insights with reservoir-scale predictions is crucial.

### 3.3. Phase-field modelling

The PF method is a leading computational approach for complex solidification and phase-transition phenomena. Based on a free-energy functional, it represents phase boundaries as diffuse interfaces of finite thickness and naturally captures their evolution when coupled to heat and mass transport, making it particularly suitable for modelling hydrate nucleation, growth, and dissociation processes.<sup>160</sup>

In 2004 Kvamme *et al.*,<sup>161</sup> implemented the PF method to investigate CO<sub>2</sub> hydrate nucleation. An order parameter distinguishing solid hydrate from liquid water and a conserved field for the concentration of CO<sub>2</sub> were introduced and coupled through a Helmholtz free-energy functional to represent a diffuse hydrate-liquid interface. Using



thermodynamic and interfacial data from experiments and MD, the PF model allowed the calculation of the nucleation barrier and steady-state nucleation rates without adjustable parameters. The critical nuclei were found to be comparable in size to the thickness of the hydrate–liquid interface, indicating that the assumptions underlying classical droplet model, namely a sharp interface and bulk solid properties within the nucleus, break down at this scale, thereby rendering such models inconsistent for describing nucleation under these conditions.

Kvamme and co-authors published several other applications of PF to investigate CO<sub>2</sub> and CH<sub>4</sub> hydrates.<sup>162</sup> These works demonstrated that the solute transport in water is the rate-limiting step for hydrate growth. It should be noted, however, that heat transport effects are not explicitly accounted for in these models, which assume isothermal conditions; consequently, the potential role of latent heat removal as a rate-limiting factor is not captured. At the same time, homogeneous nucleation was found to be unlikely because of large kinetic barriers in the formation of the complex crystal lattice. This observation suggests that homogeneous nucleation may be of limited relevance for practical applications, where heterogeneous nucleation is expected to dominate. In this context, identifying chemical structures or molecules that can act as nucleation sites may be more impactful for controlling hydrate formation. The conversion rates of CH<sub>4</sub> hydrates to CO<sub>2</sub> hydrates in the presence of liquid CO<sub>2</sub> in typical underwater gas hydrate reservoirs were also estimated using PF simulations.<sup>163</sup> Later extensions incorporated hydrodynamics and heat transport, showing that the rapid formation of new CO<sub>2</sub> hydrates releases heat that accelerates CH<sub>4</sub> dissociation.<sup>164</sup> Furthermore, pore-scale modelling demonstrated that the thickness of water films around the hydrate strongly controls conversion rates.<sup>165</sup> Finally, extensions incorporating hydrodynamics and gravity effects in PF descriptions addressed hydrate dissociation, reformation, and CH<sub>4</sub> venting risks in natural reservoirs.<sup>166</sup>

Recently, Fu *et al.*<sup>167</sup> developed a PF model to study the formation of CH<sub>4</sub> hydrates at gas–liquid interfaces under non-equilibrium conditions. They constructed a Gibbs free energy functional for CH<sub>4</sub>–water mixtures that recovers the equilibrium phase diagram and incorporates it into a PF framework to simulate hydrate growth. Their simulations reveal that the direction of growth depends on the initial concentration of CH<sub>4</sub> in water: supersaturated water leads to the growth of hydrate mainly in the liquid, while undersaturated water leads to the growth of hydrate in both the liquid and gas, which consumes a significant quantity of gas (see Fig. 9). Fu *et al.*<sup>170</sup> demonstrated that xenon (Xe) and CH<sub>4</sub> hydrates exhibit the same gas-to-liquid compositional gradient across their hydrate layers, providing evidence that Xe functions as a practical laboratory analogue for CH<sub>4</sub> hydrate. This finding is important because Xe hydrate forms under milder pressure and temperature conditions, making it easier to study experimentally.

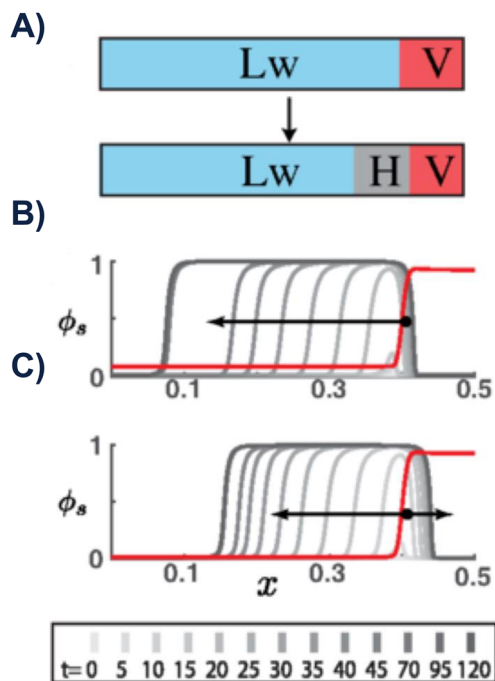


Fig. 9 A) Schematic of hydrate growth on a liquid–gas interface. 1D simulations (coordinate  $x$  is normalized) show hydrate phase-fraction profiles  $\phi_s$  (gray) over time and the initial CH<sub>4</sub> mass fraction  $\chi = m_{\text{CH}_4}/(m_{\text{CH}_4} + m_{\text{H}_2\text{O}})$  (red) for B) supersaturated and C) undersaturated liquid. The black arrow marks the growth direction; the black dot the initial gas–liquid interface. Adapted from Fu *et al.*<sup>167</sup> Copyright © 2018 American Physical Society.

PF–LBM simulations of hydrate nucleation and growth in sand sediments reproduce realistic hydrate patterns and show how porosity, water saturation, two-phase CO<sub>2</sub>–water flow, and contact angle govern hydrate distribution and permeability. These studies also provide pore-scale mechanistic insight into hydrate-induced permeability reduction and multiphase transport.<sup>171–173</sup>

The PF method is accurate but it can become computationally cumbersome when it is used to address the challenges typically encountered when investigating hydrates. These challenges include non-equilibrium multiphase thermodynamics, coupled mass–heat–momentum transport, nanoscale interfacial dynamics and nucleation, ensuring consistency with experimental data. Because the model can be applied to large systems, it is natural to expect that eventually it should be adapted to describe the impact of reservoir heterogeneity. Furthermore, in principle, the free energy functional could be formulated to incorporate, in an effective manner, insights obtained from the methods discussed above (*e.g.*, DFT, MD, and GCMC). Achieving such multiscale consistency remains challenging, but represents a promising direction for future research.

### 3.4. Population balance modelling

Understanding hydrate particle agglomeration is critical for flow assurance, where agglomeration must be



## Highlight

prevented,<sup>14,174,175</sup> as well as for emerging hydrate-based technologies, where agglomeration may be beneficial.<sup>2</sup> It is not only important to understand how hydrates adhere to each other, but also how they adhere to metal surfaces, or the surfaces of other materials used in the various technologies of interest. To describe the dynamic evolution of hydrate particle populations, PB approaches are widely employed. At the core of these approaches lies the population balance equation (PBE), which describes the time evolution of the particle-size distribution by incorporating nucleation, growth, agglomeration, and breakage. The PBE is typically solved using the sectional method (SM), kinetic Monte Carlo (kMC), the direct quadrature method of moments (DQMOM), or moment-based methods (MM).<sup>176,177</sup>

The first PBE applications to gas hydrates were carried out by Englezos *et al.*,<sup>178,179</sup> who modelled nucleation and growth of hydrates formed from CH<sub>4</sub>, C<sub>2</sub>H<sub>6</sub>, or their mixtures in water under controlled, laboratory conditions. Using the MM to solve the PBE, they showed that the overall hydrate formation rate is governed by the total surface area available for gas incorporation. This framework linked microscopic events (nucleation and growth) to macroscopic behaviour such as gas consumption. Subsequent studies have also adopted PBE-based nucleation-and-growth models to describe hydrate formation kinetics.<sup>180,181</sup>

Herri *et al.*<sup>182</sup> explicitly considered agglomeration and breakage in the PBE. Agglomeration was introduced to explain the experimentally observed crystallization behaviour of CH<sub>4</sub> hydrate at low stirring rates. At the same time, mechanical erosion and breakage were included at high stirring rates, and the simulations with erosion achieved the best agreement with the experiments.

Balakin and co-authors applied the PBE formalism to study gas hydrate particles in pipelines.<sup>183–185</sup> In 2010, they developed a PBE model to describe hydrate particle nucleation, growth, agglomeration, and breakage in turbulent flow, demonstrating that agglomeration and breakage have a strong influence on particle size.<sup>183</sup> In 2011, they coupled the PBE with computational fluid dynamics (CFD), demonstrating that particle dynamics determines the behaviour of the deposition and that the coupled CFD–PBE model yields realistic predictions.<sup>184</sup> In 2016, they presented a fully integrated CFD–PBM framework in which the particle size distribution and flow field evolved simultaneously, offering a realistic description of the hydrate agglomeration kinetics.<sup>185</sup> The coupling of PBE with CFD or CFD-like approaches is a current open research area.<sup>186–189</sup>

The DQMOM was implemented by Sampaio *et al.*<sup>190</sup> to solve a non-isothermal PBE for the formation and dissociation of gas hydrates. The modelling approach considered the mass and energy of the hydrate particles in conjunction with the gas–liquid balances and capture nucleation, growth, breakage, and agglomeration. The results showed that changes in the bulk suspension temperature, driven by slow heat transfer, strongly affect the kinetics.

Except for a few studies,<sup>185,189</sup> most of the works mentioned above focus on hydrate–water systems. Fidel-Dufour *et al.*<sup>191</sup> introduced the first PBE-based model for hydrate–oil–water systems. By tracking water droplets, hydrate particles, and agglomerates as number concentrations, their framework captured the characteristic rise and plateau of slurry viscosity during hydrate formation. Colombel *et al.*<sup>192</sup> followed a similar approach to explore different agglomeration mechanisms in water-in-oil emulsions, comparing contact-induced agglomeration *versus* shear-limited agglomeration. They concluded that porous agglomerates are responsible for an increase in viscosity and for moving the system toward the plugging zone. Moreover, they found that contact-induced models explain the experimentally observed onset of viscosity rise, but shear-limited models better predict the experimentally reported final viscosity plateau.

Most recently, Bassani *et al.*<sup>31</sup> presented a PBE framework to model the evolution of the hydrate particle/agglomerate size in a continuous flow of oil that includes nucleation, growth, and agglomeration processes simultaneously. A key aspect of the Bassani *et al.*'s model is the explicit representation of disruption and consolidation *via* a liquid-bridge mechanism, in which hydrate particles alternate between wet and dry states in response to water permeation and surface crystallisation. This wet/dry transition governs agglomeration efficiency and is itself controlled by subcooling: low subcooling favours wet, strongly agglomerating particles, while higher subcooling yields predominantly dry, weakly agglomerating particles. The



Fig. 10 Evolution of particle/agglomerate radius during hydrate formation from the two theoretical cases of the Bassani *et al.* PBE model (solved *via* MM<sup>31</sup>), compared with experiments by Kakitani *et al.*<sup>168,169</sup> solid lines indicate the full model; dashed lines indicate simplified versions. Experiments (circles) involve hydrate formation and agglomeration in oil-continuous systems with water and CH<sub>4</sub> or CH<sub>4</sub>–C<sub>3</sub>H<sub>8</sub> gas. Three subcooling-dependent behaviours occur: Trend 1 (low), Trend 2 (moderate), Trend 3 (high). Adapted with permission from Bassani *et al.*<sup>31</sup> Copyright © 2020 American Chemical Society.



model was found to be robust and predictive, offering quantitative predictions of stable agglomerate size (see Fig. 10).

PBE accuracy depends heavily on the agglomeration kernels, yet hydrate particle porosity, liquid coatings, and inhibitors often make standard kernels inadequate. Coupling PBEs with CFD is computationally costly, so PBE solutions must balance accuracy and tractability.

Taken together, CA, LBM, PF, and PBE frameworks establish the mesoscale link within a multiscale description of gas-hydrate systems, connecting molecular mechanisms to field-scale behaviour through morphology evolution, multiphase transport, and particle dynamics. Their predictive capability remains constrained by computational cost, parameter uncertainty, and the difficulty of consistently coupling heat transfer, mass transport, and phase change across scales. Advancing robust multiscale integration strategies and improving parameter calibration against molecular simulations and experiments are therefore essential for translating molecular-level insights from simulations to promote technological advancements.

## 4. Macroscale reservoir and flow assurance simulators

Macroscale gas hydrate models treat hydrates as a distributed phase within continuum frameworks, solving coupled multiphase flow, heat transfer, reaction kinetics, and geomechanics at the field scale.<sup>193</sup> The goal is to predict hydrate formation, dissociation, and transport under geological and operating conditions. These simulations are crucial for (i) reservoir modelling, assessing hydrate-bearing sediments for gas production or storage,<sup>10,194–198</sup> and (ii) flow assurance, evaluating and mitigating hydrate plugging in subsea piping systems.

### 4.1. Reservoir production modelling

At the reservoir scale, hydrate-bearing sediments are treated as coupled thermal, hydraulic, chemical, and mechanical (THCM) systems.<sup>199,200</sup> Numerous simulators predict gas production from hydrate dissociation under recovery strategies such as depressurization, thermal stimulation, chemical inhibition, and guest-molecule exchange.<sup>10</sup> Tools for gas production include TOUGH + HYDRATE,<sup>201–205</sup> HydrateResSim,<sup>206–209</sup> and CMG STARS,<sup>210–212</sup> while STOMP-HYDT-KE supports gas exchange and storage.<sup>26–28</sup> Because comparisons with experimental data remain limited, several international efforts have benchmarked hydrate simulation codes.<sup>213,214</sup> Reservoir-scale hydrate simulators solve continuum-scale partial differential equations using constitutive laws (e.g., Darcy and Fourier) and empirical correlations. Incorporating micro- and meso-scale insights remains difficult due to upscaling challenges, high computational cost, and limited experimental validation.

Overcoming these barriers is crucial for achieving more predictive, physically consistent THCM models for gas hydrates.

### 4.2. Flow assurance modelling

Flow assurance modelling predicts hydrate onset, growth, and transport in multiphase systems. It couples hydrate growth kinetics with multiphase flow simulators such as OLGA<sup>223</sup> and LedaFlow.<sup>224</sup>

OLGA applies the Colorado School of Mines Hydrate Kinetics (CSMHyK) model,<sup>225</sup> where hydrate formation rates vary exponentially with temperature, together with the Camargo–Palermo model for agglomeration and slurry formation.<sup>226</sup> LedaFlow uses a CSMHyK-like reaction model with a simplified subcooling-based kinetics and the SoFA viscosity model.<sup>227</sup> Both simulators were developed and validated primarily for oil-dominated, water-in-oil systems, and require calibration for water- or gas-dominated conditions.<sup>228–230</sup> Qu *et al.* showed that, with appropriate parameter tuning, the two simulators yield comparable predictions of hydrate transport behaviour.<sup>231</sup>

Since its integration into OLGA, CSMHyK has become a widely used hydrate model and has motivated newer transient simulators. Wang *et al.*<sup>215</sup> developed a transient tool for predicting hydrate formation, growth, and plugging—similar to OLGA–CSMHyK but extended to oil- and water-dominated regimes, antiagglomerants (AAs)/thermodynamic hydrate inhibitors (THIs) tracking, and hydrate slurry viscosity and cohesion—and successfully reproduced plugging in a real subsea pipeline (see Fig. 11). CSMHyK describes hydrate nucleation as a deterministic event once a given subcooling condition is reached. Its predictions could become more realistic if the stochasticity typical of hydrate growth and the molecular-scale features of hydrate formation observed in MD simulations were incorporated, potentially through appropriate mesoscale models. Because hydrate plugging and slurry rheology are governed by particle



Fig. 11 Predicted transient hydrate slurry relative viscosity along a subsea pipeline at 49 vol% water cut with AAs, showing a sharp rise and plug formation between 3–8 km, matching field observations. Reproduced from Wang *et al.*<sup>215</sup> Copyright © 2019 Elsevier.



**Table 1** Summary of multiscale advances and challenges in computational modelling of gas hydrates

Scale	Method	Key progress	Main challenges	Ref.
Quantum	DFT	Guest–host energetics; structural stability; cage occupancy; vibrational and elastic properties; spatial orientation of guest molecules	Functional accuracy (including dispersion)	33–35, 42–44, 55, 216
Molecular	GCMC	Adsorption isotherms; guest occupancy; spatial distributions; phase equilibria	Force-field sensitivity; limited transport properties; thermodynamic consistency limitations	63, 74–78
	MD	Nucleation pathways; growth mechanisms; additive effects; confinement effects	Time/length-scale limitations; force-field limitations; ensemble and thermodynamic control constraints	95, 96, 98, 101, 102, 110, 113, 217–221
Mesoscale	CA	Diffusion-limited growth; morphology evolution; MC-CA hybrid models; instability-driven growth; hybrid CA-FD thermal coupling	Empirical probabilistic rules; limited kinetic fidelity; scarce experimental validation	24, 131–138
	LBM	Pore-scale multiphase flow; morphology-dependent permeability; coupled thermal–hydrodynamic dissociation; realistic pore geometry	Limited applicability to pore-scale; lack of direct Darcy-scale formulation; upscaling to reservoir scale	139, 141, 142, 145, 149, 159
	PF	Diffuse-interface nucleation; non-classical barriers; transport-limited growth; thermal coupling	Computational cost; thermodynamic complexity; parameter uncertainty	161, 162, 164, 167, 222
	PBE	Particle-size evolution; agglomeration and breakage modelling; CFD-PBE coupling; slurry rheology prediction	Kernel uncertainty; CFD coupling cost; accuracy-tractability trade-off	31, 178, 184, 185
Macroscale	Reservoir modelling	THCM reservoir modelling; depressurization and thermal stimulation; guest-molecule exchange; benchmarked hydrate simulators	Empirical kinetics; upscaling limits; computational cost	10, 26, 201, 206, 213
	Flow assurance modelling	Hydrate onset and growth prediction; OLGA/LedaFlow integration; CSMHyK kinetics; transient plugging modelling	Deterministic nucleation; empirical agglomeration; parameter calibration	215, 223–225

agglomeration, consolidation, and breakage processes, further advances in flow assurance modelling are closely linked to improvements in the mechanistic description of hydrate particle properties.<sup>232</sup> In particular, enhanced PB and mesoscale models that capture agglomeration kinetics and particle-scale interactions could significantly improve predictive reliability.

## 5. Conclusions and outlook

Computational approaches are essential for understanding gas hydrate behaviour across scales. This highlight article has reviewed key micro-, meso-, and macro-scale approaches and the distinct insights each offers at its characteristic length and timescales. As summarised in Table 1, modelling approaches at each scale face distinct yet interconnected challenges, ranging from rare-event sampling at the molecular level to reliable upscaling at larger scales. Advances in molecular simulations, mesoscale computational methods, and coupled continuum frameworks are progressively addressing these limitations.

At the microscale, DFT captures atomistic-level guest–host interactions and relative stability but is computationally expensive and essentially static, with accuracy strongly dependent on the chosen XC functional, including any applied dispersion corrections.<sup>233</sup> GCMC and MD operate under realistic pressure–temperature conditions: GCMC yields equilibrium properties from the chosen interaction potential, whereas MD resolves dynamics but is constrained by timescale and force-field limitations. ML interatomic

potentials provide a promising route to address these issues.<sup>234</sup>

At the mesoscale, CA provides fast heuristic descriptions of growth, while PF yields similar behaviour at much higher computational cost; PF can calibrate CA for large-scale studies.<sup>134</sup> LBM resolves pore-scale flow but remains costly, and PBE predicts particle-size distributions and agglomeration while relying on empirical kernels. Interestingly, kMC—usually employed to solve PBEs—can also capture long-time guest diffusion in hydrate lattices *via* coarse-grained cage-to-cage hopping.<sup>235,236</sup>

Macroscale tools depend on simplified, highly upscaled models. CSMHyK, for instance, uses empirically tuned 1D formulations for oil-dominated systems with approximate chemistry, inhibitor, and plug-mechanics treatments requiring case-specific calibration. Thus, multiscale strategies are essential: micro- and meso-scale processes govern reservoir and pipeline behaviour, and macroscale simulators cannot be reliably predictive without them.

Ultimately, integrating multiscale simulation insights with molecular-scale experiments is crucial for controlling hydrate formation and growth, and ML techniques are likely to play an increasingly important role in future hydrate research.<sup>237–252</sup>

## Author contributions

Miguel Pineda: writing – original draft preparation, reviewing and editing. Anh Phan: writing – original draft preparation, reviewing and editing. Michail Stamatakis: reviewing and editing. Alberto Striolo: reviewing and editing.



## Conflicts of interest

There are no conflicts of interest to declare.

## Data availability

No new data, software, code, or research results are presented in this highlight article. Figures are adapted or reproduced from previously published research papers and are appropriately cited in the corresponding figure captions.

## Acknowledgements

Financial support was generously provided by the UK EPSRC, under grant EP/T004282/1. Generous allocations of computing time were provided by ARCHER2, the UK National Supercomputing Service (<https://www.archer2.ac.uk>), via our membership of the UK's HEC Materials Chemistry Consortium, which is funded by EPSRC (EP/X035859). AS acknowledges financial support from the Asahi Glass Chair of Chemical Engineering at the University of Oklahoma.

## Notes and references

- E. D. J. Sloan and C. A. Koh, *Clathrate Hydrates of Natural Gases*, CRC Press, 2007.
- A. Hassanpouryouzband, E. Joonaki, M. V. Farahani, S. Takeya, C. Ruppel, J. Yang, N. J. English, J. M. Schicks, K. Edlmann, H. Mehrabian, Z. M. Aman and B. Tohidi, *Chem. Soc. Rev.*, 2020, **49**, 5225–5309.
- C. I. Ratcliffe, *Energy Fuels*, 2022, **36**, 10412–10429.
- M. Khurana, Z. Yin and P. Linga, *ACS Sustainable Chem. Eng.*, 2017, **5**, 11176–11203.
- W. F. Waite, J. C. Santamarina, D. D. Cortes, B. Dugan, D. N. Espinoza, J. Germaine, J. Jang, J. W. Jung, T. J. Kneafsey, H. Shin, K. Soga, W. J. Winters and T.-S. Yun, *Rev. Geophys.*, 2009, **47**, RG4003.
- T. Yagasaki, M. Matsumoto and H. Tanaka, *J. Chem. Phys.*, 2025, **164**, 020901.
- N. Wei, J. Pei, J. Zhao, L. Zhang, S. Zhou, P. Luo, H. Li and J. Wu, *Front. Earth Sci.*, 2022, **10**, 997337.
- R. Boswell and T. S. Collett, *Energy Environ. Sci.*, 2011, **4**, 1206–1215.
- T. Collett, J.-J. Bahk, R. Baker, R. Boswell, D. Divins, M. Frye, D. Goldberg, J. Husebø, C. Koh, M. Malone, M. Morell, G. Myers, C. Shipp and M. Torres, *J. Chem. Eng. Data*, 2014, **60**, 319–329.
- Z. R. Chong, S. B. Yang, P. Babu, P. Linga and X.-S. Li, *Appl. Energy*, 2016, **162**, 1633–1652.
- H. P. Veluswamy, *ACS Appl. Energy Mater.*, 2024, **7**, 11497–11515.
- R. J. Davies, J. Yang, M. T. Ireland, C. Berndt, M. Á. Morales Maqueda and M. Huuse, *Nat. Geosci.*, 2023, **17**, 32–37.
- L. Ruffine, A. M. Tang, N. O'Neill, L. Toffin, J.-D. Paris, J. Yang, V. Georgiev, P. Fietzek, M. Giustiniani and U. Tinivella, *Earth-Sci. Rev.*, 2023, **246**, 104578.
- P. Naeiji, M. Pan, J. M. Schicks and N. J. English, *Energy Fuels*, 2025, **39**, 12001–12029.
- Z. Xin, Z. Jiang, F. Wang and Y. Zhang, *Chem. Eng. Sci.*, 2025, **306**, 121290.
- P. Wang, Y. Li, N. Sun, S. Han, X. Wang, Q. Su, Y. Li, J. He, X. Yu, S. Du, J. S. Francisco, J. Zhu and Y. Zhao, *Chem. Rev.*, 2024, **124**, 10363–10385.
- S. K. Viswanadhan, A. Singh and H. P. Veluswamy, *Gas Sci. Eng.*, 2024, **131**, 205465.
- N. N. Nguyen, *Energy Fuels*, 2023, **37**, 9771–9789.
- B. Lal and S. Nallakukkala, *Gas Hydrate in Water Treatment: Technological, Economic, and Industrial Aspects*, John Wiley & Sons, 2022.
- S. M. Montazeri and G. Kolliopoulos, *Desalination*, 2022, **537**, 115855.
- X. Wang, F. Zhang and W. Lipiński, *Sol. Energy*, 2020, **211**, 11–30.
- A. Phan, *Energy Fuels*, 2025, **39**, 10150–10164.
- Y. Zhao, M. He, Y. Du and Z. Zhang, *CrystEngComm*, 2025, **27**, 456.
- M. Pineda, A. Phan, C. A. Koh, A. Striolo and M. Stamatakis, *Cryst. Growth Des.*, 2023, **23**, 4222–4239.
- C. L. Bassani, M. Engel and A. K. Sum, *J. Chem. Phys.*, 2024, **160**, 190901.
- M. D. White, *STOMP-HYDT-KE: A Numerical Simulator for the Production of Natural Gas Hydrate Using Guest Molecule Exchange with CO<sub>2</sub> and N<sub>2</sub>*, Pacific Northwest National Laboratory Technical Report PNNL-22130, 2012.
- C. M. R. Yonkofski, J. A. Horner and M. D. White, *J. Nat. Gas Sci. Eng.*, 2016, **35**, 1480–1489.
- A. Palodkar and A. K. Jana, *Sci. Rep.*, 2019, **9**, 18901.
- C. L. Bassani, A. Melchuna, A. Cameirão, J.-M. Herri, A. K. Sum and R. E. Morales, *Ind. Eng. Chem. Res.*, 2019, **58**, 14446–14461.
- C. L. Bassani, A. K. Sum, J.-M. Herri, R. E. Morales and A. Cameirão, *Ind. Eng. Chem. Res.*, 2020, **59**, 2123–2144.
- C. L. Bassani, C. Kakitani, J. M. Herri, A. K. Sum, R. E. M. Morales and A. Cameirão, *Ind. Eng. Chem. Res.*, 2020, **59**, 15357–15377.
- C. L. Bassani, J.-M. Herri, A. Cameirão, R. E. M. Morales and A. K. Sum, *Ind. Eng. Chem. Res.*, 2021, **60**, 14004–14012.
- X. Zhu, A. Guerra, P. Servio and A. D. Rey, *Sci. Rep.*, 2023, **13**, 1907.
- K. Schmidt, M. Mohamed, S. J. D. Sofla, A. Rey and P. Servio, *Energy Fuels*, 2025, **39**, 9157–9169.
- A. Cabrera-Ramírez, D. J. Arismendi-Arrieta, A. Valdés and R. Prosmi, *ChemPhysChem*, 2021, **22**, 359–369.
- J. Witte, N. Mardirossian, J. B. Neaton and M. Head-Gordon, *J. Chem. Theory Comput.*, 2017, **13**, 2043–2052.
- J. Klimeš and A. Michaelides, *J. Chem. Phys.*, 2012, **137**, 120901.
- S. Grimme, A. Hansen, J. G. Brandenburg and C. Bannwarth, *Chem. Rev.*, 2016, **116**, 5105–5154.
- J. Hermann, R. A. DiStasio Jr and A. Tkatchenko, *Chem. Rev.*, 2017, **117**, 4714–4758.



- 40 M. G. Medvedev, I. S. Bushmarinov, J. Sun, J. P. Perdew and K. A. Lyssenko, *Science*, 2017, **355**, 49–52.
- 41 P. Hohenberg and W. Kohn, *Phys. Rev. A*, 1964, **136**, B864–B871.
- 42 T. M. Vlasic, P. Servio and A. D. Rey, *AIP Adv.*, 2016, **6**, 085317.
- 43 S. M. Daghash, P. Servio and A. D. Rey, *Mol. Simul.*, 2019, **45**, 1524–1537.
- 44 S. L. Mathews, P. D. Servio and A. D. Rey, *Cryst. Growth Des.*, 2020, **20**, 5947–5955.
- 45 Z. M. Jendi, P. Servio and A. D. Rey, *Cryst. Growth Des.*, 2015, **15**, 5301–5309.
- 46 X. Zhu, A. D. Rey and P. Servio, *Energy Fuels*, 2022, **36**, 10591–10600.
- 47 X. Zhu, A. D. Rey and P. Servio, *Can. J. Chem. Eng.*, 2023, **101**, 639–650.
- 48 S. B. Hansen and R. W. Berg, *Appl. Spectrosc. Rev.*, 2009, **44**, 168–179.
- 49 K. R. Ramya, G. V. Pavan Kumar and A. Venkatnathan, *J. Chem. Phys.*, 2012, **136**, 174305.
- 50 T. M. Vlasic, P. D. Servio and A. D. Rey, *J. Phys. Chem. B*, 2019, **123**, 936–947.
- 51 H.-C. Wang, X.-L. Zhu, J.-W. Cao, X.-L. Qin, Y.-C. Yang, T.-X. Niu, Y.-B. Lu and P. Zhang, *New J. Phys.*, 2020, **22**, 093066.
- 52 J. M. Skelton, L. A. Burton, A. J. Jackson, F. Oba, S. C. Parker and A. Walsh, *Phys. Chem. Chem. Phys.*, 2017, **19**, 12452–12465.
- 53 J. S. Tse, M. L. Klein and I. R. McDonald, *J. Phys. Chem.*, 1983, **87**, 4198–4203.
- 54 J. Jia, Y. Liang, T. Tsuji, S. Murata and T. Matsuoka, *Sci. Rep.*, 2017, **7**, 1290.
- 55 A. Cabrera-Ramírez, D. J. Arismendi-Arrieta, A. Valdés and R. Prosimiti, *ChemPhysChem*, 2020, **21**, 2618–2628.
- 56 F. Izquierdo-Ruiz, A. Otero-de-la Roza, J. Contreras-García, O. Prieto-Ballesteros and J. Recio, *Materials*, 2016, **9**, 777.
- 57 A. Valdés, D. J. Arismendi-Arrieta and R. Prosimiti, *J. Phys. Chem. C*, 2015, **119**, 3945–3956.
- 58 M. Pérez-Rodríguez, A. Vidal-Vidal, J. M. Míguez, F. J. Blas, J.-P. Torré and M. M. Piñeiro, *Phys. Chem. Chem. Phys.*, 2017, **19**, 3384–3393.
- 59 D. J. Arismendi-Arrieta, A. Valdés and R. Prosimiti, *Chem. – Eur. J.*, 2018, **24**, 9353–9363.
- 60 K. A. Udachin, C. I. Ratcliffe and J. A. Ripmeester, *J. Phys. Chem. B*, 2001, **105**, 4200–4204.
- 61 S. Takeya, K. A. Udachin, I. L. Moudrakovski, R. Susilo and J. A. Ripmeester, *J. Am. Chem. Soc.*, 2010, **132**, 524–531.
- 62 Y. Park, D.-Y. Kim, J.-W. Lee, D.-G. Huh, K.-P. Park, J. Lee and H. Lee, *Proc. Natl. Acad. Sci. U. S. A.*, 2006, **103**, 12690–12694.
- 63 N. Qiu, X. Bai, N. Sun, X. Yu, L. Yang, Y. Li, M. Yang, Q. Huang and S. Du, *J. Phys. Chem. B*, 2018, **122**, 9724–9737.
- 64 P. E. Brumby, D. Yuhara, D. T. Wu, A. K. Sum and K. Yasuoka, *Fluid Phase Equilib.*, 2016, **413**, 242–248.
- 65 N. I. Papadimitriou, I. N. Tsimpanogiannis, I. G. Economou and A. K. Stubos, *J. Chem. Eng. Data*, 2016, **61**, 2886–2896.
- 66 N. I. Papadimitriou, I. N. Tsimpanogiannis, I. G. Economou and A. K. Stubos, *J. Chem. Thermodyn.*, 2018, **117**, 128–137.
- 67 H. Henley and A. Lucia, *J. Nat. Gas Sci. Eng.*, 2015, **26**, 446–452.
- 68 J. Qin, C. Hartmann and W. Kuhs, *Proceedings of the 8th International Conference on Gas Hydrates (ICGH-8)*, Beijing, China, 2015.
- 69 J. Qin and W. F. Kuhs, *AIChE J.*, 2013, **59**, 2155–2167.
- 70 A. Klapproth, E. Goreschnik, D. Staykova, H. Klein and W. F. Kuhs, *Can. J. Phys.*, 2003, **81**, 503–518.
- 71 T. C. Hansen, A. Falenty and W. F. Kuhs, *J. Chem. Phys.*, 2016, **144**, 054301.
- 72 A. Valdés, A. Cabrera-Ramírez and R. Prosimiti, *J. Comput. Chem.*, 2023, **44**, 1587–1598.
- 73 S. Alavi, P. Dornan and T. K. Woo, *ChemPhysChem*, 2008, **9**, 911–919.
- 74 I. N. Tsimpanogiannis and I. G. Economou, *J. Supercrit. Fluids*, 2018, **134**, 51–60.
- 75 I. N. Tsimpanogiannis, I. G. Economou and A. K. Stubos, *J. Chem. Eng. Data*, 2020, **65**, 1289–1299.
- 76 S. N. Chakraborty and L. D. Gelb, *J. Phys. Chem. B*, 2012, **116**, 2183–2197.
- 77 N. I. Papadimitriou, I. N. Tsimpanogiannis, A. T. Papaioannou and A. K. Stubos, *J. Phys. Chem. C*, 2008, **112**, 10294–10302.
- 78 M. H. Waage, T. J. H. Vlugt and S. Kjelstrup, *J. Phys. Chem. B*, 2017, **121**, 7336–7350.
- 79 J. H. van der Waals and J. C. Platteeuw, in *Clathrate Solutions*, ed. I. Prigogine and S. A. Rice, John Wiley & Sons, Inc., 1958, vol. 2, pp. 1–57.
- 80 J. H. Yoon, T. Kawamura, Y. Yamamoto and T. Komai, *J. Phys. Chem. A*, 2004, **108**, 5057–5059.
- 81 E. Kim, S. Lee, J. D. Lee and Y. Seo, *Fuel*, 2016, **164**, 237–244.
- 82 S. Lee, S. Park, Y. Lee and Y. Seo, *Chem. Eng. J.*, 2013, **225**, 636–640.
- 83 S. Lee, Y. Lee, J. Lee, H. Lee and Y. Seo, *Environ. Sci. Technol.*, 2013, **47**, 13184–13190.
- 84 H. Lee, Y. Seo, Y.-T. Seo, I. L. Moudrakovski and J. A. Ripmeester, *Angew. Chem., Int. Ed.*, 2003, **42**, 5048–5051.
- 85 D.-L. Zhong, Z. Li, Y.-Y. Lu, J.-L. Wang and J. Yan, *Appl. Energy*, 2015, **158**, 133–141.
- 86 M. Ota, K. Morohashi, Y. Abe, M. Watanabe, R. L. J. Smith and H. Inomata, *Energy Convers. Manage.*, 2005, **46**, 1680–1691.
- 87 Y.-T. Seo, H. Lee and J.-H. Yoon, *J. Chem. Eng. Data*, 2001, **46**, 381–384.
- 88 Y.-T. Seo and H. Lee, *J. Phys. Chem. B*, 2001, **105**, 10084–10090.
- 89 T. Uchida, R. Ohmura and A. Hori, *J. Phys. Chem. C*, 2008, **112**, 4719–4724.
- 90 M. G. Martin, A. P. Thompson and T. M. Nenoff, *J. Chem. Phys.*, 2001, **114**, 7174–7181.
- 91 M. D. Jager, *PhD thesis*, Colorado School of Mines, 2001.
- 92 R. Sun and Z. Duan, *Geochim. Cosmochim. Acta*, 2005, **69**, 4411–4424.



- 93 J. L. Cox, *Natural gas hydrates: Properties, occurrence and recovery*, Butterworth Publishers, Stoneham, MA, USA, 1982.
- 94 L. Ballard and E. D. Sloan Jr, *Fluid Phase Equilib.*, 2004, **216**, 257–270.
- 95 M. R. Walsh, C. A. Koh, E. D. Sloan, A. K. Sum and D. T. Wu, *Science*, 2009, **326**, 1095–1098.
- 96 J. Liu, J. Hou, J. Xu, H. Liu, G. Chen and J. Zhang, *Energy*, 2017, **120**, 698–704.
- 97 A. Phan, M. Stamatakis, C. A. Koh and A. Striolo, *J. Colloid Interface Sci.*, 2023, **649**, 185–193.
- 98 L. C. Jacobson, W. Hujo and V. Molinero, *J. Phys. Chem. B*, 2010, **114**, 13796–13807.
- 99 L. C. Jacobson and V. Molinero, *J. Am. Chem. Soc.*, 2011, **133**, 6458–6463.
- 100 M. R. Walsh, G. T. Beckham, C. A. Koh, E. D. Sloan, D. T. Wu and A. K. Sum, *J. Phys. Chem. C*, 2011, **115**, 21241–21248.
- 101 A. Phan, H. Schlösser and A. Striolo, *Chem. Eng. J.*, 2021, **418**, 129423.
- 102 A. Phan and A. Striolo, *Energy Fuels*, 2023, **37**, 6002–6011.
- 103 A. Striolo, A. Phan and M. R. Walsh, *Curr. Opin. Chem. Eng.*, 2019, **25**, 57–66.
- 104 A. Farhadian, A. Phan, Z. Taheri Rizzi, A. Shaabani, E. Sadeh, M. Mohammad-Taheri, M. A. Aminolroayaei, A. Mohammadi, N. Sayyari and F. Wang, *Green Chem.*, 2025, **27**, 4523–4539.
- 105 X. Cai, J. Worley, A. Phan, M. Salvalaglio, C. Koh and A. Striolo, *J. Colloid Interface Sci.*, 2024, **658**, 1–11.
- 106 Z. Zhang, P. G. Kusalik, N. Wu, C. Liu and Y. Zhang, *Energy*, 2022, **257**, 124738.
- 107 K. B. Yu and A. O. Yazaydin, *J. Phys. Chem. C*, 2020, **124**, 11015–11022.
- 108 E. D. Sloan Jr and F. Fleyfel, *AIChE J.*, 1991, **37**, 1281–1291.
- 109 R. Radhakrishnan and B. L. Trout, *J. Chem. Phys.*, 2002, **117**, 1786–1796.
- 110 G. Guo, Y. Zhang, Y. J. Zhao, K. Refson and G. Shan, *J. Chem. Phys.*, 2004, **121**, 1542–1547.
- 111 Z. Zhang, N. Wu, C. Liu, X. Hao, Y. Zhang, K. Gao, B. Peng, W. Zheng, C. Tang and G. Guo, *China Geol.*, 2022, **5**, 330–344.
- 112 E. A. Mastny, C. A. Miller and J. J. de Pablo, *J. Chem. Phys.*, 2008, **129**, 034701.
- 113 G.-J. Guo, Y.-G. Zhang and H. Liu, *J. Phys. Chem. C*, 2007, **111**, 2595–2606.
- 114 J. M. Schicks and J. A. Ripmeester, *Angew. Chem., Int. Ed.*, 2004, **43**, 3310–3313.
- 115 F. Fleyfel and J. P. Devlin, *J. Phys. Chem.*, 1991, **95**, 3811–3815.
- 116 D. K. Staykova, W. F. Kuhs, A. N. Salamatin and T. Hansen, *J. Phys. Chem. B*, 2003, **107**, 10299–10311.
- 117 C. Moon, R. W. Hawtin and P. M. Rodger, *Faraday Discuss.*, 2007, **136**, 367–382.
- 118 C. Moon, P. C. Taylor and P. M. Rodger, *J. Am. Chem. Soc.*, 2003, **125**, 4706–4707.
- 119 D. Daniel-David, F. Guerton, C. Dicharry, J.-P. Torré and D. Broseta, *Chem. Eng. Sci.*, 2015, **132**, 118–127.
- 120 X. Cai, J. Worley, A. Phan, M. Salvalaglio, C. A. Koh and A. Striolo, *J. Colloid Interface Sci.*, 2024, **658**, 1–11.
- 121 V. K. Michalis, J. Costandy, I. N. Tsimpanogiannis, A. K. Stubos and I. G. Economou, *J. Chem. Phys.*, 2015, **142**, 044501.
- 122 I. N. Tsimpanogiannis, L. D. Peristeras, A. K. Stubos, I. G. Economou and V. K. Michalis, *J. Chem. Phys.*, 2025, **163**, 234502.
- 123 X. Cai, Y. Zhang, M. Salvalaglio, P. Linga and A. Striolo, *Chem. Eng. J.*, 2026, **527**, 171463.
- 124 R. W. Hawtin, D. Quigley and P. M. Rodger, *Phys. Chem. Chem. Phys.*, 2008, **10**, 4853–4864.
- 125 J. Zhang, R. W. Hawtin, Y. Yang, E. Nakagawa, M. Rivero, S. K. Choi and P. M. Rodger, *J. Phys. Chem. B*, 2008, **112**, 10608–10618.
- 126 L. C. Jacobson, W. Hujo and V. Molinero, *J. Am. Chem. Soc.*, 2010, **132**, 11806–11811.
- 127 L. C. Jacobson, W. Hujo and V. Molinero, *J. Phys. Chem. B*, 2009, **113**, 10298–10307.
- 128 L. C. Jacobson and V. Molinero, *J. Phys. Chem. B*, 2010, **114**, 7302–7311.
- 129 X. Cai, M. Salvalaglio and A. Striolo, *Proc. Natl. Acad. Sci. U. S. A.*, 2026, **123**, e2521343123.
- 130 A. Phan and A. Striolo, *Energy Fuels*, 2023, **37**, 6002–6011.
- 131 K. Reuther and M. Rettenmayr, *Comput. Mater. Sci.*, 2014, **95**, 213–220.
- 132 D. Raabe, *Annu. Rev. Mater. Res.*, 2002, **32**, 53–76.
- 133 T. Buanes, B. Kvamme and A. Svandal, *J. Cryst. Growth*, 2006, **287**, 491–494.
- 134 T. Buanes, B. Kvamme and A. Svandal, *J. Math. Chem.*, 2009, **46**, 811–819.
- 135 D. V. Alexandrov and P. Galenko, *J. Appl. Phys.*, 2024, **136**, 055103.
- 136 L. Jiang, N. Xu, Q. Liu, Z. Cheng, Y. Liu and J. Zhao, *Cryst. Growth Des.*, 2021, **20**, 8148–8161.
- 137 S. Jahangiri and F. Varaminian, *J. Mol. Liq.*, 2024, **406**, 125021.
- 138 L. Jiang, N. Xu, Q. Liu, Z. Cheng, Y. Liu and J. Zhao, *Cryst. Growth Des.*, 2020, **20**, 8148–8161.
- 139 Z. Li, L. Zhao, Z. Cao, S. Wu, B. Dindoruk and G. Quin, *Geoenergy Sci. Eng.*, 2024, **241**, 213066.
- 140 S. Chen and G. D. Doolen, *Annu. Rev. Fluid Mech.*, 1998, **30**, 339–364.
- 141 Q. Kang, D. Zhang, P. C. Lichtner and I. N. Tsimpanogiannis, *Geophys. Res. Lett.*, 2004, **31**, L21604.
- 142 Q. Wang, D. Han, Z. Wang, Q. Ma and D. Wang, *Chem. Eng. J.*, 2016, **366**, 133–140.
- 143 D. Corak, T. Barth, S. Høiland, T. Skodvin, R. Larsen and T. Skjetne, *Desalination*, 2011, **278**, 268–274.
- 144 G. Zyllyftari, J. W. Lee and J. F. Morris, *Chem. Eng. Sci.*, 2013, **95**, 148–160.
- 145 D. H. Kang, K. Y. Yu, T. S. Kim and J. Jang, *Geophys. Res. Lett.*, 2016, **43**, 9018–9025.
- 146 J. Hou, Y. Ji, K. Zhou, Y. Liu and B. Wei, *Int. J. Heat Mass Transfer*, 2018, **126**, 416–424.
- 147 Y. Ji, T. J. Kneafsey, J. Hou, J. Zhao, C. Liu, T. Guo, B. Wei, E. Zhao and Y. Bai, *Fuel*, 2022, **321**, 124013.



- 148 Y. Li, T. Xu, X. Xin, B. Yang, Y. Xia, Y. Zang, Y. Yuan and H. Zhu, *J. Hydrol.*, 2024, **635**, 131178.
- 149 X. Chen, R. Verma, D. Nicolas Espinoza and M. Prodanović, *Water Resour. Res.*, 2018, **54**, 600–608.
- 150 J. Sun, Z. Zhang, D. Wang, C. Liu, H. Lu and K. Song, *Mar. Pet. Geol.*, 2021, **123**, 104749.
- 151 L. Zhang, C. Zhang, K. Zhang, L. Zhang, J. Yao, H. Sun and Y. Yang, *Water Resour. Res.*, 2019, **55**, 8422–8444.
- 152 J. Yang, X. Dai, Q. Xu, Z. Liu, C. Zan, W. Long and L. Shi, *Chem. Eng. J.*, 2021, **423**, 130226.
- 153 J. Yang, Q. Xu, Z. Liu and L. Shi, *Chem. Eng. J.*, 2022, **430**, 132786.
- 154 J. Yang, Q. Xu, Z. Liu, L. Shi, T. Lei and K. H. Luo, *Chem. Eng. Sci.*, 2023, **275**, 118742.
- 155 J. Yang, B. Dong, W. Ping, F. Geng, L. Zhang, Y. Quin, C. Cheng and W. Li, *Energy*, 2023, **266**, 126489.
- 156 X. Li, W. Cui, T. Ma, Z. Ma, J. Liu and Q. Wang, *Energy*, 2023, **278**, 127984.
- 157 Z. Li, Z. Wang and H. Ji, *Water*, 2024, **16**, 2734.
- 158 J. Yang, Q. Xu, X. Kou, G. Wang, T. Lei, Y. Wang, X. Li and K. H. Luo, *Innovation Energy*, 2024, **1**, 100015.
- 159 P. Hassard, I. Turner and D. Lester, *Transp. Porous Media*, 2023, **150**, 675–707.
- 160 I. Steinbach, *Modell. Simul. Mater. Sci. Eng.*, 2009, **17**, 073001.
- 161 B. Kvamme, A. Graue, L. Gránásy, G. Tóth, T. Pusztai and G. Tegze, *Phys. Chem. Chem. Phys.*, 2004, **6**, 2327–2334.
- 162 A. Svandal, B. Kvamme, L. Gránásy, T. Pusztai, T. Buanes and J. Hove, *J. Cryst. Growth*, 2006, **287**, 486–490.
- 163 G. Tegze, L. Gránásy and B. Kvamme, *Phys. Chem. Chem. Phys.*, 2007, **9**, 3104–3111.
- 164 B. Kvamme, M. Qasim, K. Baig, P.-F. Kivelä and J. Bauman, *Int. J. Greenhouse Gas Control*, 2014, **29**, 263–278.
- 165 K. Baig, B. Kvamme, T. Kuznetsova and J. Bauman, *AIChE J.*, 2015, **61**, 3944–3957.
- 166 M. Qasim, B. Kvamme and K. Baig, *Int. J. Geol.*, 2011, **5**, 48–52.
- 167 X. Fu, L. Cueto-Felgueroso and R. Juanes, *Phys. Rev. Lett.*, 2018, **120**, 144501.
- 168 C. Kakitani, *PhD thesis*, Federal University of Technology-Paraná (UTFPR), Curitiba, Brazil, 2019.
- 169 C. Kakitani, D. C. Marques, M. A. M. Neto, A. Teixeira, L. S. Valim, R. E. M. Morales and A. K. Sum, *Proceedings of the Offshore Technology Conference*, Houston, Texas, USA, 2020, pp. 1–8.
- 170 X. Fu, W. F. Waite, L. Cueto-Felgueroso and R. Juanes, *Geochem., Geophys., Geosyst.*, 2018, **20**, 2462–2472.
- 171 A. Fukumoto, K. Kamada, T. Sato, H. Oyama, H. Torii, F. Kiyono, J. Nagao, N. Temma and H. Narita, *J. Nat. Gas Sci. Eng.*, 2018, **50**, 269–281.
- 172 A. J. Yamaguchi, T. Sato, A. Nono, S. A. Scheiderei and T. Tobase, *Mar. Syst. Ocean Technol.*, 2021, **16**, 157–167.
- 173 S. Lu, A. J. Yamaguchi, K. Kobayashi, T. Sato and T. Tobase, *Int. J. Greenh. Gas Con.*, 2022, **121**, 103789.
- 174 Y. Song, L. Yang, W. Zhao, J. Liu, M. Yang, Y. Li, Y. Liu and Q. Li, *Renew. Sustain. Energy Rev.*, 2014, **31**, 778–791.
- 175 S. Mokhatab, R. J. Wilkens and K. J. Leontaritis, *Energy Sources, Part A*, 2007, **29**, 39–45.
- 176 J. Solsvik and H. A. Jakobsen, *Chem. Soc. Rev.*, 2015, **36**, 510–520.
- 177 H. M. Omar and S. Rohani, *Cryst. Growth Des.*, 2017, **17**, 4028–4041.
- 178 P. Englezos, N. Kalogerakis, P. D. Dholabhai and P. R. Bishnoi, *Chem. Eng. Sci.*, 1987, **42**, 2647–2658.
- 179 P. Englezos, N. Kalogerakis, P. D. Dholabhai and P. R. Bishnoi, *Chem. Eng. Sci.*, 1987, **42**, 2659–2666.
- 180 B. ZareNezhad, M. Mottahedin and F. Varaminian, *Chem. Eng. Sci.*, 2015, **137**, 447–457.
- 181 M. S. Khatami and A. Shahsavand, *Energy Fuels*, 2018, **32**, 8131–8144.
- 182 J. M. Herri, J. S. Pic, F. Gruy and M. Cournil, *AIChE J.*, 1999, **45**, 590.
- 183 B. V. Balakin, A. C. Hoffmann and P. Kosinski, *AIChE J.*, 2010, **56**, 2052.
- 184 B. V. Balakin, A. C. Hoffmann and P. Kosinski, *Chem. Eng. Sci.*, 2011, **66**, 755–765.
- 185 S. Balakin, B. V. Lo, P. Kosinski and A. C. Hoffmann, *Chem. Eng. Sci.*, 2016, **153**, 45–57.
- 186 G. Song, Y. Li, W. Wang, K. Jiang, Z. Shi and S. Yao, *J. Pet. Eng.*, 2018, **169**, 393–404.
- 187 C. Yu, L. Wang, C. Han, Y. Jing, J. Li, W. Wang, M. Du, X. Song and L. Zhang, *J. Mech. Sci. Technol.*, 2023, **36**, 3477–3486.
- 188 C. Yu, C. Han, L. Wang, J. Jing, Y. Li, W. Wang, M. Du and X. Song, *J. Mech. Sci. Technol.*, 2023, **37**, 5159–5171.
- 189 Y. Gao, Y. Xu, K. Song, Q. Li, H. Yao, H. Chen, W. Wang and Y. Li, *J. Pipeline Sci. Eng.*, 2023, **3**, 100104.
- 190 T. P. Sampaio, F. W. Tavares and P. L. C. Lage, *Chem. Eng. Sci.*, 2017, **163**, 234–254.
- 191 A. Fidel-Dufour, F. Gruy and J.-M. Herri, *Chem. Eng. Sci.*, 2006, **61**, 505–515.
- 192 E. E. Colombel, P. Gateau, L. L. Barré', F. F. Gruy and T. Palermo, *Oil Gas Sci. Technol. Rev.*, 2009, **64**, 629–636.
- 193 J. K. S. Sayani, B. Lal and S. R. Pedapati, *Arch. Comput. Method Eng.*, 2022, **29**, 2171–2207.
- 194 F. Li, Q. Yuan, T. Li, Z. Li, C. Sun and G. Chen, *Chin. J. Chem. Eng.*, 2019, **27**, 2062–2073.
- 195 Z. Yin, Z. R. Chong, H. K. Tan and P. Linga, *Chin. J. Chem. Eng.*, 2016, **35**, 1362–1387.
- 196 M. Huang, L. Wu, F. Ning, J. Wang, X. Dou, L. Zhang, T. Liu and G. Jiang, *Nat. Gas Ind. B*, 2023, **10**, 114–129.
- 197 X. S. Li, C. G. Xu, Y. Zhang, X. K. Ruan, G. Li and Y. Wang, *Appl. Energy*, 2016, **172**, 286–322.
- 198 X. Ruan, X.-S. Li and C. G. Xu, *J. Nat. Gas Sci. Eng.*, 2021, **85**, 103713.
- 199 R. Zhou, B. Bai, G. Cai and X. Chen, *Comput. Geotech.*, 2024, **167**, 106057.
- 200 L. Zhang, Q. Wu, B. Li, Q. Hao and H. Zhang, *Appl. Math. Model.*, 2024, **129**, 88–111.
- 201 G. J. Moridis, *User's Manual for the HYDRATE v1.5 Option of TOUGH+ v1.5: A Code for the Simulation of System Behavior in Hydrate-Bearing Geologic Media*, Lawrence Berkeley National Laboratory Technical Report LBNL-6869E, 2014.



- 202 L. Chen, Y. Feng, T. Kogawa, J. Okajima, A. Komiya and S. Maruyama, *Energy*, 2018, **143**, 128–140.
- 203 S. Dhakal and I. Gupta, *J. Nat. Gas Sci. Eng.*, 2020, **75**, 103154.
- 204 N. Wei, C. Li, X. Zhao, H. Li, L. Zhang, J. Zhao, B. Kvamme and R. B. Coffin, *Front. Earth Sci.*, 2024, **12**, 1444690.
- 205 Y. Liu, J. Liu, W. Jia, Y. Bai, J. Hou, H. Xu, E. Zhao, L. Chen, T. H. J. Guo, L. Zhang and E. Chuvilin, *Nat. Gas Ind. B*, 2024, **11**, 274–290.
- 206 G. J. Moridis, M. B. Kowalsky and K. Pruess, *HydrateResSim User's Manual: A Numerical Simulator for Modeling the Behavior of Hydrates in Geologic Media*, Earth Sciences Division, Lawrence Berkeley National Laboratory, Berkeley, CA, 2005.
- 207 P. Zhang, S. Tian, Y. Zhang, G. Li, W. Zhang, W. A. Khan and L. Ma, *Energy*, 2021, **220**, 119549.
- 208 P. Zhang, Y. Zhang, W. Zhang and S. Tian, *Energy*, 2022, **238**, 121738.
- 209 I. K. Gamwo and Y. Liu, *Ind. Eng. Chem. Res.*, 2010, **49**, 5231–5245.
- 210 S. Zhang, Y. Ma, Z. Xu, Y. Zhang, X. Liu, X. Zhong, G. Tu and C. Chen, *Energy*, 2024, **303**, 131998.
- 211 J. Liu, Z. Xu, H. Li, X. Li and S. Fan, *Energy Fuels*, 2023, **37**, 18996–19010.
- 212 T. K. Lin, M. Dahyar, M. J. Lee and B. Z. Hsieh, *J. Taiwan Inst. Chem. Eng.*, 2020, **114**, 115–124.
- 213 J. W. Wilder, G. J. Moridis, S. J. Wilson, M. Kurihata, M. D. White, Y. Masuda, B. J. Anderson, T. S. Collet, R. B. Hunter, H. Narita, M. Pooladi-Darvish, K. Rose and R. Boswell, *Proceedings of the 6th International Conference on Gas Hydrates (ICGH 2008)*, Vancouver, British Columbia, Canada, 2008, pp. 1–14.
- 214 M. D. White, T. J. Kneafsey, Y. Seol, W. F. Waite, S. Ushida, J. S. Lin, E. M. Myshakin, X. Gai, S. Gupta, M. T. Reagan, A. F. Queiruga, S. Kimoto and I. Participants, *Mar. Pet. Geol.*, 2020, **120**, 104566.
- 215 Y. Wang, C. A. Koh, J. White, Z. Patel and L. E. Zerpa, *Fuel*, 2019, **252**, 458–468.
- 216 S. Patchkovskii and J. S. Tse, *Proc. Natl. Acad. Sci. U. S. A.*, 2003, **100**, 14645–14650.
- 217 L. C. Jacobson and V. Molinero, *J. Am. Chem. Soc.*, 2011, **133**, 6458–6463.
- 218 J. Vatamanu and P. G. Kusalik, *J. Phys. Chem. B*, 2008, **112**, 2399–2404.
- 219 J. Vatamanu and P. G. Kusalik, *Phys. Chem. Chem. Phys.*, 2010, **12**, 15065–15072.
- 220 M. Matsumoto, *J. Phys. Chem. Lett.*, 2010, **1**, 1552–1556.
- 221 S. J. Cox, D. J. F. Taylor, T. G. A. Youngs, A. K. Soper, T. S. Totton, R. G. Chapman, M. Arjmandi, M. G. Hodges, N. T. Skipper and A. Michaelides, *J. Am. Chem. Soc.*, 2018, **140**, 3277–3284.
- 222 F. Cheng, H. Lyu, W. Liu, X. Sun, Z. You, Y. Li and Y. Tian, *Comput. Geotech.*, 2025, **188**, 107532.
- 223 D. Turner, J. Boxall, S. Yang, D. M. Kleehammer, C. A. Koh, K. T. Miller, E. D. Sloan, Z. Xu, P. Matthews and L. Talley, *5th International Conference on Gas Hydrates*, Trondheim, Trondheim, Norway, 2005, pp. 1188–1197.
- 224 T. Danielson, K. Bansal, R. Hansen and E. Leporcher, *Proceedings of the 12th International Conference on Multiphase Production Technology'05*, Barcelona, Spain, 2005, pp. 477–492.
- 225 L. E. Zerpa, E. D. Sloan, A. K. Sum and C. A. Koh, *J. Pet. Sci. Eng.*, 2012, **98-99**, 122–129.
- 226 R. Camargo and T. Palermo, *Proceedings of the fourth international conference on gas hydrates*, Yokohama, Japan, 2002, pp. 880–885.
- 227 T. Palermo and E. Tournis, *Ind. Eng. Chem. Res.*, 2015, **54**, 4526–4534.
- 228 T. B. Charlton, M. Di Lorenzo, L. E. Zerpa, C. A. Koh, M. L. Johns, E. F. May and Z. M. Aman, *Energy Fuels*, 2018, **32**, 1012–1023.
- 229 S. Zhang, L. Shang, L. Zhou and Z. Lv, *Energy Fuels*, 2022, **36**, 1747–1775.
- 230 Y. Wang, C. A. Koh, J. A. Dapena and L. E. Zerpa, *J. Nat. Gas Sci. Eng.*, 2018, **48**, 126–134.
- 231 A. Qu, L. F. R. Dalla, L. E. Zerpa, T. Parlermo, K. Mateen, A. Fidel-Dufour and C. A. Koh, *Energies*, 2024, **17**, 6101.
- 232 R. Castrejon-Miranda, J. G. Delgado-Linares and C. A. Koh, *Fuel*, 2026, **409**, 137808.
- 233 S. J. Cox, M. D. Towler, D. Alfè and A. Michaelides, *J. Chem. Phys.*, 2014, **140**, 174703.
- 234 I. Batatia, P. Benner, Y. Chiang, A. M. Elena, D. P. Kovács, J. Riebesell, X. R. Advincula, M. Asta, M. Avaylon, W. J. Baldwin, F. Berger, N. Bernstein, A. Bhowmik, F. Bigi, S. M. Blau, V. Cărare, M. Ceriotti, S. Chong, J. P. Darby, S. De, F. Della Pia, V. L. Deringer, R. Elijošius, Z. El-Machachi, E. Fako, F. Falcioni, A. C. Ferrari, J. L. A. Gardner, M. J. Gawkowski, A. Genreith-Schriever, J. George, R. E. A. Goodall, J. Grandel, C. P. Grey, P. Grigorev, S. Han, W. Handley, H. H. Heenen, K. Hermansson, C. H. Ho, S. Hofmann, C. Holm, J. Jaafar, K. S. Jakob, H. Jung, V. Kapil, A. D. Kaplan, N. Karimitari, J. R. Kermodé, P. Kourtis, N. Kroupa, J. Kullgren, M. C. Kuner, D. Kuryla, G. Liepuoniutė, C. Lin, J. T. Margraf, I.-B. Magdău, A. Michaelides, J. H. Moore, A. A. Naik, S. P. Niblett, S. W. Norwood, N. O'Neill, C. Ortner, K. A. Persson, K. Reuter, A. S. Rosen, L. A. M. Rosset, L. L. Schaaf, C. Schran, B. X. Shi, E. Sivonxay, T. Stenczel, C. Sutton, V. Svahn, T. D. Swinburne, J. Tilly, C. van der Oord, S. Vargas, E. Varga-Umbrich, T. Vegge, M. Vondrák, Y. Wang, W. C. Witt, T. Wolf, F. Zills and G. Csányi, *J. Chem. Phys.*, 2025, **163**, 184110.
- 235 B. Peters, N. E. R. Zimmermann, G. T. Beckham, J. W. Tester and B. L. Trout, *J. Am. Chem. Soc.*, 2008, **130**, 17342–17350.
- 236 L.-S. Chu, D. T. Wu and S. T. Lin, *J. Phys. Chem. C*, 2019, **123**, 11233–11243.
- 237 H. Xu, Z. Jiao, Z. Zhang, M. Huffman and Q. Wang, *Comput. Chem. Eng.*, 2021, **151**, 107358.
- 238 A. J. Yamaguchi, T. Sato, T. Tobase, X. Wei, L. Huang, J. Zhang, J. Bian and T.-Y. Liu, *Proceedings of the ASME OMAE*, 2022, p. V010T11A001.



- 239 Z. Yu and H. Tian, *Energies*, 2022, **15**, 4719.
- 240 A. J. Yamaguchi, T. Sato, T. Tobase, X. Wei, L. Huang, J. Zhang, J. Bian and T.-Y. Liu, *Fuel*, 2023, **334**, 126678.
- 241 E. L. Gjelsvik, M. Fossen and K. Tøndel, *Fuel*, 2023, **334**, 126696.
- 242 M. Hosseini and Y. Leonenko, *Renew. Sustain. Energy Rev.*, 2023, **173**, 113103.
- 243 D. Tian, S. Yang, Y. Gong, M. Geng, Y. Li and G. Hu, *Geoenergy Sci. Eng.*, 2023, **223**, 211564.
- 244 H. Osei, C. B. Bavoh and B. Lal, *ACS Omega*, 2024, **9**, 4210–4228.
- 245 Y. Zhang, Z. Song, Y. Lin, Q. Shi, Y. Hao, Y. Fu, J. Wu and Z. Zhang, *J. Phys.: Condens. Matter*, 2024, **36**, 015101.
- 246 V. Dhamu, M. Xiao, M. F. Qureshi and P. Linga, *Energy*, 2024, **313**, 133802.
- 247 H. Li, H. Sun, J. Chen, B. Chen, D. Zhong and M. Yang, *Energy Fuels*, 2024, **38**, 23320–23335.
- 248 G. S. Patel and A. K. Jana, *Energy Fuels*, 2024, **38**, 16272–16285.
- 249 L. Wan, P. Cao and J. Sheng, *Langmuir*, 2024, **40**, 22058–22067.
- 250 M. R. Atta, A. F. Al-Mahmodi, B. Lal, H. Abdulrab and S. F. Khor, *Energy Fuels*, 2025, **39**, 18287–18310.
- 251 V. Dhamu, X. Mengqi, M. F. Qureshi, Z. Yin, A. K. Jana and P. Linga, *Energy*, 2024, **290**, 129947.
- 252 A. N. Rehman, C. B. Bavoh, M. Y. Khan, M. Ansari and B. Lal, *Fuel*, 2025, **381**, 133650.

